

1 Feasibility of keeping Mars warm with nanoparticles

2
3 **Authors:** Samaneh Ansari¹, Edwin S. Kite^{2,*}, Ramses Ramirez³, Liam J. Steele⁴, Hooman
4 Mohseni¹

5 6 **Affiliations:**

7 1. Department of Electrical and Computer Engineering, Northwestern University; Evanston,
8 IL.

9 2. Department of the Geophysical Sciences, University of Chicago; Chicago, IL.

10 3. Department of Physics, University of Central Florida; Orlando, FL.

11 4. European Center for Medium-Range Weather Forecasts; Reading, UK.

12 * Corresponding author, kite@uchicago.edu

13
14 **Abstract:** One-third of Mars' surface has shallow-buried H₂O, but it is currently too cold for
15 use by life (Feldman et al. 2004, Dundas et al. 2018). Proposals to warm Mars using
16 greenhouse gases require a large mass of ingredients that are rare on Mars' surface.
17 However, we show here that artificial aerosols made from materials that are readily
18 available at Mars' surface—specifically, conductive nanorods that are 9 μm long—could
19 warm Mars 10³ times more effectively than the best gases. Such nanorods forward-scatter
20 sunlight and efficiently block upwelling thermal infrared. Similar to the natural dust of Mars,
21 they are swept high into Mars' atmosphere, allowing delivery from the near-surface. For a
22 particle lifetime of 10 years, two climate models indicate that release at 30 liters/sec
23 would globally warm Mars by >30 K and start to melt the ice. Therefore, if nanorods can be
24 made at scale on Mars, then the barrier to warming of Mars appears to not be as high as
25 previously thought.

26
27 **One-sentence summary:** Warming Mars with artificial aerosols appears to be feasible.

28
29 **Main text:** Dry river valleys cross Mars's once-habitable surface (Mangold et al. 2021,
30 Grotzinger et al. 2014), but today the icy soil is too cold for Earth-derived life (McKay 2014).
31 Streams may have flowed as recently as 600 Kyr ago (Dickson et al. 2023), hinting at a planet
32 on the cusp of habitability. Many methods have been proposed to warm Mars' surface by
33 closing the spectral windows, centered around wavelengths (λ) 22 μm and 10 μm, through
34 which the surface is cooled by thermal infrared radiation upwelling to space (McKay et al.
35 1991, Marinova et al. 2005, Wordsworth et al. 2019). Modern Mars has a thin (~6 mbar) CO₂
36 atmosphere that provides only ~5 K greenhouse warming via absorption in the 15 μm band
37 (Haberle 2013), and Mars apparently lacks enough condensed or mineralized CO₂ to restore
38 a warm climate (Jakosky & Edwards 2018). The spectral windows can be closed using
39 artificial greenhouse gases (e.g. chloroflourocarbons) (Gerstell et al. 2001, Marinova et al.
40 2005), but this would require volatilizing ~100,000 megatons of fluorine, which is sparse on
41 the Mars surface. An alternative approach is suggested by natural Mars dust aerosol.
42 Mars dust is almost all ultimately sourced from slow comminution (indirect estimate $O(3)$
43 liters/second, Kite & Mayer 2017) of iron-rich minerals on Mars' surface. Due to its small size

44 (1.5 μm effective radius), Mars dust is lofted to high altitude (altitude of peak dust mass
45 mixing ratio 15-25 km), is always visible in the Mars sky, and is present up to >60 km altitude
46 (McCleese et al. 2010; Kahre et al. 2017, and references therein). Natural Mars dust aerosol
47 lowers daytime surface temperature (e.g., Streeter et al. 2019), but this is due to
48 compositional and geometric specifics that can be modified in the case of engineered dust.
49 For example, a nanorod about half as long as the wavelength of upwelling thermal infrared
50 radiation should interact strongly with that radiation (Van Vleck et al. 1947). Consider a
51 9- μm long conductive (iron) nanorod with a $\sim 60:1$ aspect ratio, not much smaller than
52 commercially available glitter. Finite-difference time domain calculations (Supplementary
53 Methods) show that such nanorods, randomly oriented due to Brownian motion (Seinfeld &
54 Pandis 2006), would strongly scatter and absorb upwelling thermal infrared in the spectral
55 windows, and forward-scatter sunlight down to the surface, leading to net warming (Fig. 1,
56 Figs. S1-S4). Results are robust to changing particle material type, cross-sectional shape, and
57 mesh resolution, and change as expected with particle length and aspect ratio (Figs. S5-S8).
58 The maximum extinction cross section scales as (rod length)². The calculated thermal
59 infrared scattering is near-isotropic (Fig. 1), which favors surface warming (Forget &
60 Pierrehumbert 1997). Such nanorods would settle >100 \times more slowly in the Mars
61 atmosphere than natural Mars dust (Seinfeld & Pandis 2006) (Supplementary Methods),
62 implying that once the particles are lifted into the air they would be lofted to high altitude
63 and have a long atmospheric lifetime.

64
65 This motivates calculating surface warming (K) as a function of (artificial) aerosol column
66 density (kg/m^2). The MarsWRF global climate model is suitable for such a calculation
67 (Richardson et al. 2007, Toigo et al. 2012, Kite et al. 2021). Following many previous works
68 (Conrath 1975, Ramirez and Kasting 2017, Ramirez 2017, Turbet et al. 2020, Kite et al. 2021),
69 we prescribe a layer of aerosol, and calculate the resulting steady-state warming
70 (Supplementary Methods). Our calculation does not include dynamic transport of aerosol,
71 but includes realistic topography, seasonal forcing, and surface thermophysical properties
72 and albedo. The 3D model output (Fig. 2, Figs. S10-S15) shows that nanorod column density
73 $400 \text{ mg}/\text{m}^2$ yields surface temperatures and pressures permitting extensive summertime
74 (i.e., the warmest ~ 70 sols period each year) liquid water in locations with shallow ground-
75 ice. This is >2000 \times more effective, on a warming-per-unit-mass-in-the-atmosphere basis,
76 than the current state of the art (Marinova et al. 2005) (Supplementary Methods).
77 Temperatures experienced by subsurface ice will be lower due to insulation by soil. Water
78 ice at <1 m depth is almost ubiquitous poleward of $\pm 50^\circ$ latitude (blue lines in Fig. 2)
79 (Feldman et al. 2004). H_2O ice is present further equatorward (Dundas et al. 2021), but is
80 insulated beneath >1 m soil cover and so would not melt unless the annual average surface
81 temperature is raised close to 273K.

82
83 The greenhouse effect depends on the temperature difference between the top of
84 the optically thick IR emitting/absorbing layer and that of the planet surface; higher clouds
85 have a bigger ΔT relative to the surface (due to adiabatic cooling) and so give a stronger
86 greenhouse effect. Therefore, the results depend on both artificial-dust-layer-top height and

87 column density (Pierrehumbert 2010). Fig. 2c shows the results varying the layer-top height
 88 between ~ 35 km and ~ 28 km. The minimum column density for significant warming
 89 (Fig. 2c) can be estimated by setting optical depth in the spectral window (τ_{win}) to unity and
 90 solving the following expression for column density M_c (mg/m^2) (e.g. Ramirez and Kasting
 91 2017):

$$\tau_{win} = 3 Q_{eff} M_c / (4 r \rho) \quad (1)$$

92
93

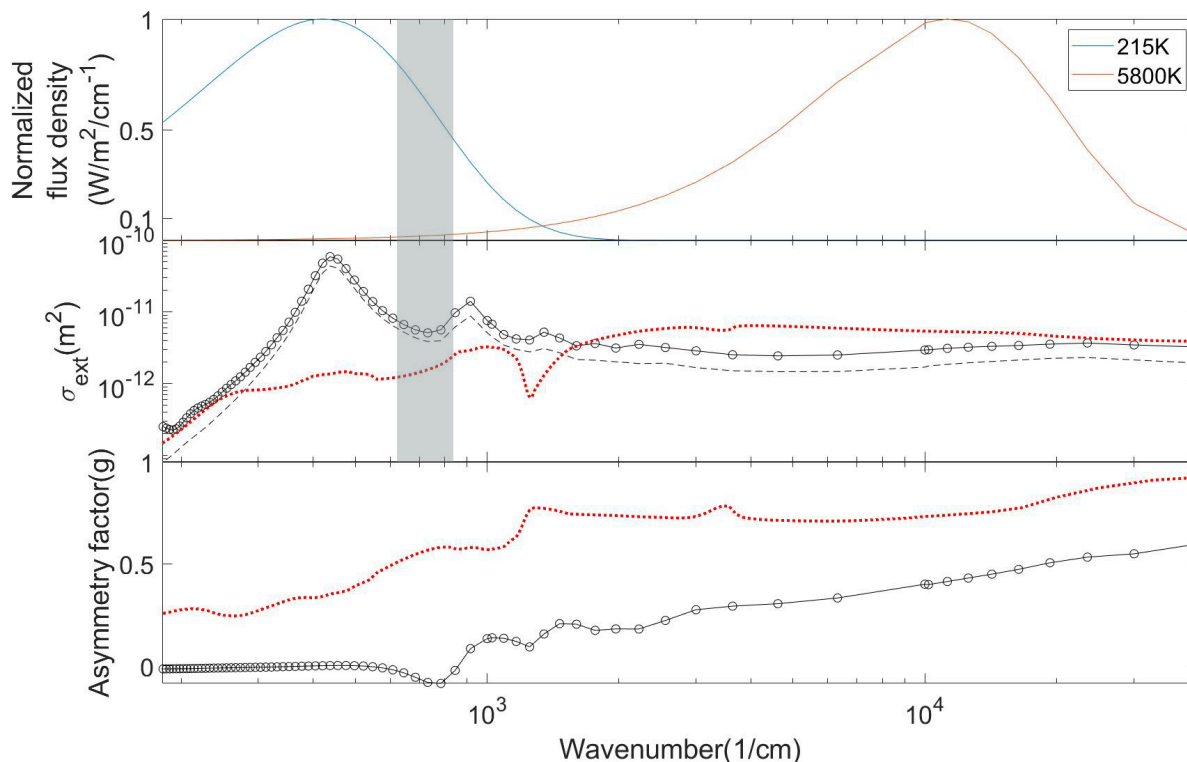


Fig. 1. Orientation-averaged optical properties of a $9 \mu\text{m}$ -long Fe nanorod with cross-section $0.16 \mu\text{m} \times 0.16 \mu\text{m}$, calculated using a 3D Finite-Difference Time-Domain (FDTD) approach. Top panel: Planck functions (normalized flux density, $\text{W}/\text{m}^2/\mu\text{m}$) for 215 K (Mars thermal emission now, red) and 6000 K (insolation, blue). For context, the CO_2 band is overlain (gray shading) at $12\text{-}16 \mu\text{m}$. Middle panel: Solid black line corresponds to total extinction, dotted black line to scattering. Lower panel shows scattering asymmetry. Also shown are wavelength dependence of total extinction and asymmetry factor for natural dust assuming a log-gaussian particle size distribution centered on $2.5 \mu\text{m}$ (Wolff & Clancy 2003) (red dotted lines).

94 Here, Q_{eff} is the wavenumber-dependent extinction efficiency, ρ is the nanorod particle
 95 density ($8 \text{ g}/\text{cc}$), and r is the effective nanorod particle radius (the radius of a sphere
 96 of equivalent volume, $0.38 \mu\text{m}$). Here, Q_{eff} is the ratio of the extinction cross-section in
 97 the spectral window (about one-half the maximum cross-section, i.e. $3 \times 10^{-11} \text{ m}^2$, from Fig. 1)
 98 to the geometric cross-section of the equivalent sphere, and is ≈ 60 . This gives a minimum

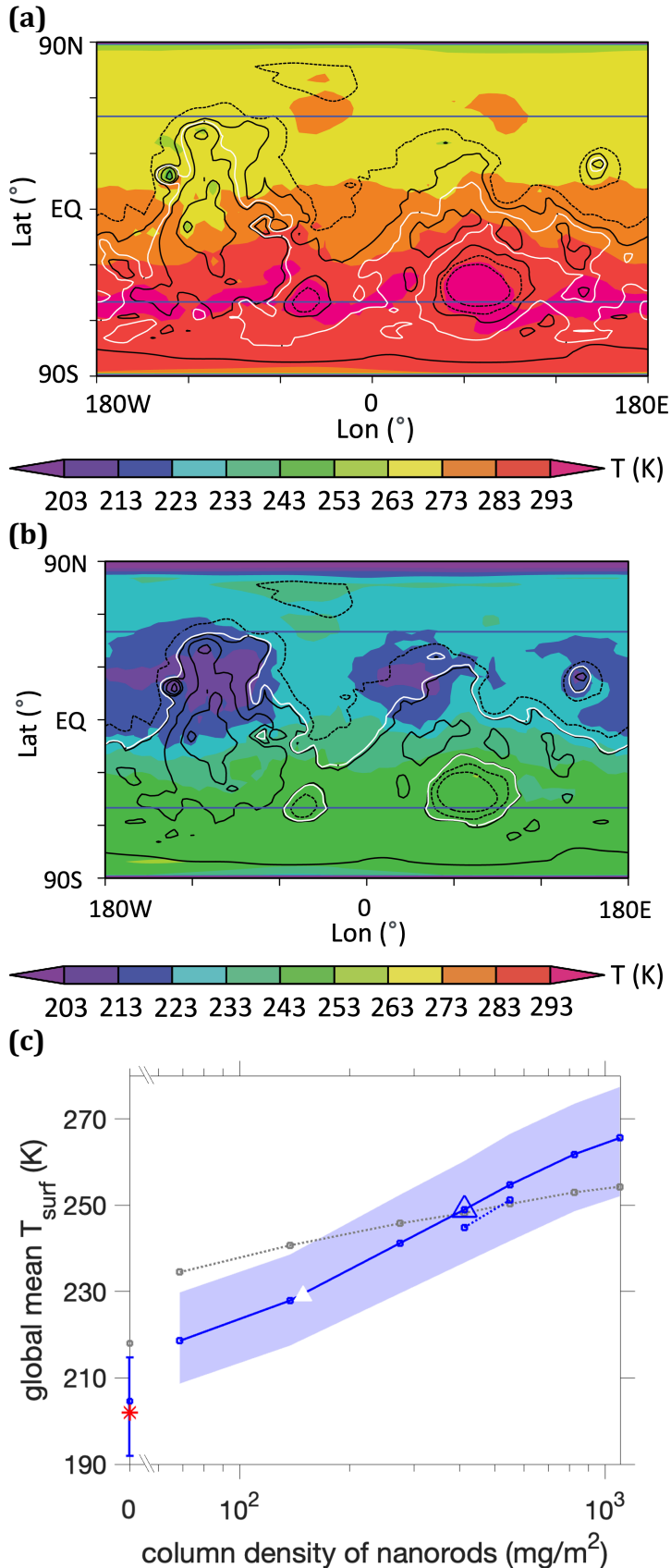


Fig. 2. Warm-season temperatures (K) (color shading) on (a) Mars with addition of $\sim 400 \text{ mg/m}^2$ of nanorods, (b) control case. This corresponds to the average surface temperature during the warmest 36° of solar longitude (~ 70 days) of the year. White contour corresponds to 610 Pa mean pressure level. Black contours correspond to topographic elevation in m (dashed: -5 km and -2 km, solid: 0 km, +2km, and +5 km). Blue lines: approximate latitudinal (equatorward) extent of ice at <1 m depths. Results do not include CO_2 outgassing from within polar ice, which would cause further warming. (c) Dependence of planet-averaged surface warming on nanorod column mass. Blue line corresponds to 3-D results, varying layer-top height between ~ 35 km (solid line) and ~ 28 km (dashed line). The blue envelope corresponds to the modeled seasonal range in global mean T_{surf} . Gray corresponds to 1-D results (see text for details). Blue triangle corresponds to panel (a), blue square at 0 mg/m^2 corresponds to no-nanorod case (panel b), and white triangle marks onset of warm-season temperatures above the freezing point of water at 50°S . Symbols on y-axis are temperatures for the no-nanorod case, with the red asterisk corresponding to observed Mars value. More detail is shown in Figs. S10-S17.

99 column density (M_c) of 70 mg/m². At 400 mg/m², the volumetric density of nanorods,
100 10 cm⁻³, gives a Brownian coagulation timescale (for 0.1-10 μm diameter spheres, for 100%
101 accretion efficiency) \approx 6 years (Seinfeld & Pandis 2006). This timescale estimate has
102 significant uncertainties; for example, actual accretion efficiency may be less, for example
103 because monodisperse particles of uniform composition (e.g. nanorods) may carry similar
104 charges and thus repel each other (Federova et al. 2014). On Mars, particles would be taken
105 up by dry deposition and by transient CO₂ ice, and re-released to the atmosphere by dust
106 lifting. Initial release (after manufacture) could be from a pipe extending 10-100m above
107 the surface, as Mars turbulent updrafts strengthen with distance from the surface
108 (Spiga et al. 2010). For an effective particle lifetime of 10 years, sustaining the warming
109 shown in Fig. 2a requires particle fountaining at an average rate of 30 liters/sec (1 liter/sec
110 corresponds to the flow of one standard garden sprinkler). This lifetime is consistent
111 with one-pass fall-out of \sim 0.1 μm-radius particles (Murphy et al. 1990), and particle lifetime
112 might be greatly extended if the particles are engineered to self-loft (Keith 2010, Daerden
113 et al. 2015, Azadi et al. 2021), further reducing the sustaining mass flux; however, effective
114 particle lifetime remains a major uncertainty in our model.
115

116 As a check on the 3-D results, we ran a 1-D model using annual-average Mars insolation
117 (Supplementary Methods). This also predicts 250 K global temperature for \sim 400 mg/m²
118 nanorods (Fig. 2c, Figs. S16-S17). For further increases in nanorod loading, the 1-D model
119 predicts global temperatures 10K lower than does the 3-D model. This may be due to
120 differences in the vertical temperature structure of the two models.
121

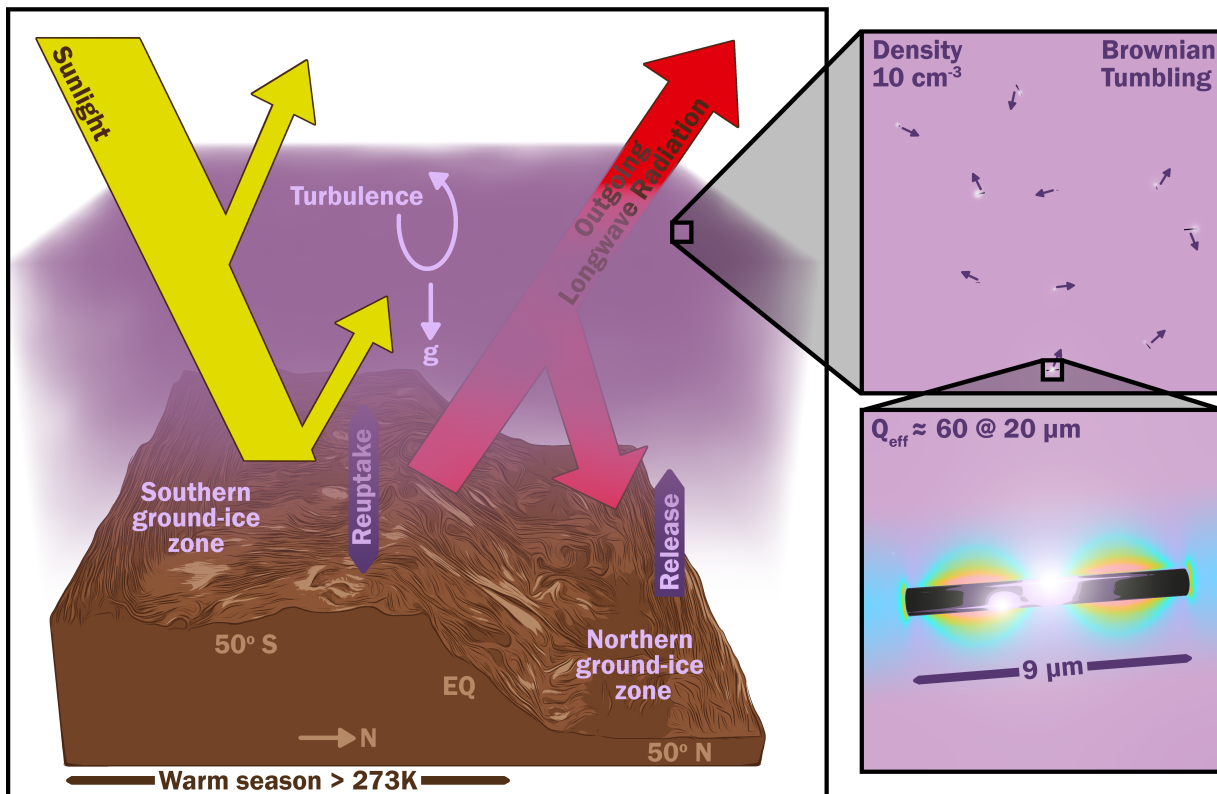
122 Even in the warmed climate, the south pole is cold enough for seasonal CO₂ condensation.
123

124 Within months of warming Mars, the atmospheric pCO₂ increases by \sim 20% as CO₂ ice
125 sublimates, a positive warming feedback. On a warmed Mars, atmospheric pressure will
126 further increase by a factor of 2-20 as adsorbed CO₂ desorbs (Buhler & Piqueux 2021),
127 and polar CO₂ ice (Phillips et al. 2011) is volatilized on a timescale that could be as long as
128 centuries. This will further increase the area that is suitable for liquid water (Dickson et al.
129 2023). However, raising Mars' temperature, by itself, is not sufficient to make the planet's
130 surface habitable for oxygenic photosynthetic life: significant barriers remain. For example,
131 remediating perchlorate-rich soil might require bioremediation by perchlorate-reducing
132 bacteria, which yield molecular oxygen as a natural byproduct (Davila et al. 2013).
133

134 The results from this relatively simple workflow are subject to several uncertainties
135 that motivate more sophisticated modeling. As one of several examples, modeling of coupled
136 dust flow and ice nucleation on Mars is currently at an early stage (Bertrand et al. 2020).
137 Modeling the effect of nanorods as ice nuclei - which could either be a positive or a negative
138 feedback, depending on the size and altitude of the resulting water ice cloud particles
139 and their precipitation efficiency - is additional motivation to study this coupling. A thin
140 coating on the nanorods could alter their hydrophobicity level, and potentially the ice

141 nucleation, and might also protect against oxidation. The optimal location(s) for particle
 142 fountaining require further research. Release into the ascending limb of the Hadley cell
 143 should allow dispersal in both hemispheres. The radiative effect of water vapor feedback is
 144 unambiguously positive. Tests varying nanorod size, composition, and shape suggest that
 145 further improvements to warming effectiveness are possible (Figs. S7-S8.).
 146

147 With these caveats in mind, Fig. 2c allows a first estimate of how much surface material
 148 would be needed to supply the fountains. For surface-material density 2 g/cc,
 149 and $\text{Fe}_2\text{O}_3/\text{Fe}_3\text{O}_4$ content of ~ 10 wt% (e.g. Hurowitz et al. 2017), raising the surface
 150 temperature to that shown in Fig. 2a over 10 years would require processing 4×10^7 m³/yr
 151 surface material to obtain 1×10^6 m³/yr of metal, corresponding to a prismatic mine of half-
 152 width 350m and side-wall slope 20°, lengthening by 500m per year. This is much easier
 153 than the current state-of-the-art (Marinova et al. 2005), as Mars surface material likely has
 154 <10 ppmw F. However, even this reduced material-processing demand still corresponds
 155 to 5×10^{-3} of Earth's iron/steel budget, and this defines a major manufacturing problem that
 156 remains to be solved. Processing of surface material into nanoparticles might use lenses or
 157 mirrors to concentrate sunlight for vacuum evaporation, followed by colloidal growth.
 158 Synthetic biology (e.g. magnetite nanorods) is a possible alternative (Lang et al. 2007). Metal
 159 3D printing of parts (e.g. Relativity's Stargate) and/or assembly on Mars (e.g. Blue Alchemist)
 160 might reduce launch costs (Salmi 2019).
 161



162
 163 **Fig. 3.** Graphical summary. Figure credit: Aaron M. Geller, Northwestern, CIERA + IT-RCDS.
 164

165 Although nanorods could warm Mars (Fig. 2c, Fig. 3), both the benefits and potential costs of
166 this course of action are currently uncertain. For example, if Mars' soil contains irreparable
167 compounds toxic to all Earth-derived life (this can be tested with Mars Sample Return), then
168 the benefit of warming Mars is nil. On the other hand, if a photosynthetic biosphere can be
169 established on the surface of Mars, perhaps with the aid of synthetic biology, that might
170 increase the Solar System's capacity for human flourishing. On the costs side, if Mars has
171 extant life, then study of that life could have great benefits that warrant robust protections
172 for its habitat. More immediately, further research into nanoparticle design and manufacture
173 coupled with modeling of their interaction with the climate could reduce the expense of this
174 method. Examples include Mars-pressure wind-tunnel experiments for nanorod and dust re-
175 uptake and release rate from realistic rough surfaces (including icy surfaces), and
176 mesoscale/large-eddy-simulation modeling of nanorod dispersal and lofting. In addition to
177 the nanorod warming option and the no-action option, cost-benefit calculations should also
178 consider local-warming methods, such as silica aerogel tiling (Wordsworth et al. 2019).
179

180 More work is needed on the very-long-term sustainability of a warmed Mars. Atmospheric
181 escape to space would take at least 300 Myr to deplete the atmosphere at the present-day
182 rate (Jakosky et al. 2018). However, if the ground ice observed at meters to tens of meters
183 depth is underlain by empty pore space, then excessive warming over centuries could allow
184 water to drain away, requiring careful management of long-term warming. Subsurface
185 exploration by electromagnetic methods could address this uncertainty regarding how much
186 water remains on Mars deep underground (Grimm 2002).
187

188 The efficiency of nanoparticle warming suggests that any entity with the goal of strong
189 planet-scale warming would use this approach. This suggests polarization as a
190 technosignature for cold terrestrial worlds with geodynamos.
191

192 Nanoparticle warming, by itself, is not sufficient to make the planet's surface habitable again.
193 Nevertheless, our study suggests that nanoparticle warming may be of interest to
194 the nanophotonics and planetary science communities, among others, and that further
195 investigation might be fruitful.
196

197 **Acknowledgements.**

198 We thank M. Turbet, C. Willard, M.A. Mischna, A. Geller, M.I. Richardson, C. Lee, A. Noblet, and
199 the PlanetWRF development team. This research was supported in part through the
200 computational resources and staff contributions provided for the Quest high performance
201 computing facility at Northwestern University which is jointly supported by the Office of the
202 Provost, the Office for Research, and Northwestern University Information Technology, and
203 with resources provided by the University of Chicago's Research Computing Center.
204

205 **Author contributions.** ESK conceived research. SA, ESK, RR, LJS, and HM designed research.
206 SA, ESK, and RR carried out research. ESK drafted the manuscript. SA, ESK, RR, LJS, and HM
207 edited the manuscript and contributed to the final manuscript.
208

209 **Data and materials availability.** All data needed to evaluate the conclusions in the paper
210 are present in the paper and/or the Supplementary Materials. Additional data, for example
211 full 3D climate model output files, are stored at Zenodo (doi:10.5281/zenodo.8352416).
212 FDTD: 3D Electromagnetic Simulator is commercial code (Lumerical). The MarsWRF source
213 code can be made available by Aeolis Research pending scientific review and a completed
214 Rules of the Road agreement. Requests for the MarsWRF source code should be submitted
215 to mir@aeolisresearch.com.
216

217 **References.**

218
219 Azadi, M., G. A. Popov, Z. Lu, A. G. Eskenazi, A. Ji Won Bang, M. F. Campbell, H. Hu, and
220 I. Bargatin. Controlled levitation of nanostructured thin films for sun-powered near-space
221 flight. *Science Advances* 7, no. 7 (2021): eabe1127.
222

223 Bertrand, T. R. J. Wilson, M. A. Kahre, R. Urata, and A. Kling. Simulation of the 2018 global
224 dust storm on Mars using the NASA Ames Mars GCM: a multitracer approach. *J. Geophys. Res.*
225 - Planets 125, no. 7 (2020): e2019JE006122.
226

227 Buhler, P. B., and S. Piqueux. Obliquity-Driven CO₂ Exchange Between Mars' Atmosphere,
228 Regolith, and Polar Cap. *J. Geophys. Res. - Planets* 126, no. 5 (2021): e2020JE006759.
229

230 Conrath, B.J., Thermal structure of the Martian atmosphere during the dissipation of the dust
231 storm of 1971. *Icarus*, 24(1) (1975), 36-46.
232

233 Davila, A. F., D. Willson, J. D. Coates, and C. P. McKay. Perchlorate on Mars: a chemical hazard
234 and a resource for humans. *Intl. Journal of Astrobiology* 12, (2013): 321-325.
235

236 Daerden, F., J. A. Whiteway, L. Neary, L. Komguem, M. T. Lemmon, N. G. Heavens, B. A. Cantor,
237 E. Hébrard, and M. D. Smith. A solar escalator on Mars: Self-lifting of dust layers by radiative
238 heating. *Geophys. Res. Lett.* 42, no. 18 (2015): 7319-7326.
239

240 Dickson, J.L., Palumbo, A.M., Head, J.W., Kerber, L., Fassett, C.I. and Kreslavsky, M.A.. Gullies
241 on Mars could have formed by melting of water ice during periods of high
242 obliquity. *Science*, 380, 6652 (2023), pp.1363-1367.
243

244 Dundas, C. M., A. M. Bramson, L. Ojha, J. J. Wray, M. T. Mellon, S. Byrne, A. S. McEwen et al.
245 Exposed subsurface ice sheets in the Martian mid-latitudes. *Science* 359, 6372 (2018): 199-
246 201.
247

248 Dundas, C. M., M. T. Mellon, S. J. Conway, I. J. Daubar, K. E. Williams, L. Ojha, J. J. Wray et al.
249 Widespread exposures of extensive clean shallow ice in the midlatitudes of Mars. *J. Geophys.*
250 *Res. - Planets* 126, no. 3 (2021): e2020JE006617.
251

252 Fedorova, A. A., F. Montmessin, A. V. Rodin, O. I. Korablev, A. Määttänen, L. Maltagliati, and
253 J-L. Bertaux. Evidence for a bimodal size distribution for the suspended aerosol particles on
254 Mars. *Icarus* 231 (2014): 239-260.
255

256 Feldman, W. C., T. H. Prettyman, S. Maurice, J. J. Plaut, D. L. Bish, D. T. Vaniman, M. T. Mellon
257 et al. Global distribution of near-surface hydrogen on Mars. *J. Geophys. Res. - Planets* 109, E9
258 (2004).
259

260 Forget, F., and R. T. Pierrehumbert. Warming early Mars with carbon dioxide clouds that
261 scatter infrared radiation. *Science* 278, no. 5341 (1997): 1273-1276.
262

263 Gerstell, M. F., J. S. Francisco, Y. L. Yung, C. Boxe, and E. T. Aaltonen. Keeping Mars warm with
264 new super greenhouse gases. *Proc. Natl. Acad. Sci. USA* 98, no. 5 (2001): 2154-2157.
265

266 Grimm, R. E. Low-frequency electromagnetic exploration for groundwater on Mars. *Journal*
267 *of Geophysical Research: Planets* 107, no. E2 (2002): 1-1.
268

269 Grotzinger, J. P., D. Y. Sumner, L. C. Kah, K. Stack, S. Gupta, L. Edgar, D. Rubin et al. A habitable
270 fluvio-lacustrine environment at Yellowknife Bay, Gale Crater, Mars. *Science* 343, no. 6169
271 (2014): 1242777.
272

273 Haberle, R. M. Estimating the power of Mars' greenhouse effect. *Icarus* 223, 1 (2013): 619-
274 620.
275

276 Hurowitz, J. A., J. P. Grotzinger, W. W. Fischer, S. M. McLennan, R. E. Milliken, N. Stein,
277 A. R. Vasavada et al. Redox stratification of an ancient lake in Gale crater, Mars. *Science* 356,
278 no. 6341 (2017): eaah6849.
279

280 Jakosky, B. M., and C. S. Edwards. Inventory of CO₂ available for terraforming Mars. *Nature*
281 *Astronomy* 2(8) (2018): 634-639.
282

283 Kahre, M. A., J. R. Murphy, C. E. Newman, R. J. Wilson, B. A. Cantor, M. T. Lemmon, and
284 M. J. Wolff. The Mars dust cycle. in Haberle, R., et al. (Eds.), 2017, *The Atmosphere and*
285 *Climate of Mars* (2017): 295, Cambridge University Press.
286

287 Keith, D. W. Photophoretic levitation of engineered aerosols for geoengineering. *Proc. Natl.*
288 *Acad. Sci. USA* 107 (2010): 16428-16431.
289

290 Kite, E. S., and D. P. Mayer. Mars sedimentary rock erosion rates constrained using crater
291 counts, with applications to organic-matter preservation and to the global dust cycle. *Icarus*
292 286 (2017): 212-222.
293

294 Kite, E. S., L. J. Steele, M. A. Mischna, and M. I. Richardson. Warm early Mars surface enabled
295 by high-altitude water ice clouds. *Proceedings of the National Academy of Sciences* 118, no.
296 18 (2021): e2101959118.

297
298 Jakosky, B. M., D. Brain, M. Chaffin, S. Curry, J. Deighan, J. Grebowsky, J. Halekas et al. Loss of
299 the Martian atmosphere to space: Present-day loss rates determined from MAVEN
300 observations and integrated loss through time. *Icarus* 315 (2018): 146-157.
301
302 Lang, C., D. Schüler, and D. Faivre. Synthesis of magnetite nanoparticles for bio- and
303 nanotechnology. *Macromolecular bioscience* 7, 2 (2007): 144-151.
304
305 McKay, C.P., Toon, O.B. and Kasting, J.F., Making Mars habitable. *Nature*, 352, 6335 (1991),
306 489-496.
307
308 McKay, C.P. (2014), Requirements and limits for life in the context of exoplanets. *Proc. Natl.*
309 *Acad. Sci. USA*, 111(35), 12628-12633.
310
311 Mangold, N., S. Gupta, O. Gasnault, G. Dromart, J. D. Tarnas, S. F. Sholes, B. Horgan et al.
312 Perseverance rover reveals an ancient delta-lake system and flood deposits at Jezero crater,
313 Mars. *Science* 374, no. 6568 (2021): 711-717.
314
315 Marinova, M. M., C. P. McKay, and H. Hashimoto. Radiative-convective model of warming
316 Mars with artificial greenhouse gases. *J. Geophys. Res. - Planets* 110, no. E3 (2005).
317
318 McCleese, D. J., N. G. Heavens, J. T. Schofield, W. A. Abdou, J. L. Bandfield, S. B. Calcutt,
319 P. G. J. Irwin et al. Structure and dynamics of the Martian lower and middle atmosphere as
320 observed by the Mars Climate Sounder: Seasonal variations in zonal mean temperature, dust,
321 and water ice aerosols. *J. Geophys. Res. - Planets* 115, no. E12 (2010).
322
323 Murphy, J. R., O. B. Toon, R. M. Haberle, and J. B. Pollack. Numerical simulations of the decay
324 of Martian global dust storms. *J. Geophys. Res. Solid Earth* 95 (B9) (1990): 14629-14648.
325
326 Phillips, R.J., Davis, B.J., Tanaka, K.L., Byrne, S., Mellon, M.T., Putzig, N.E., Haberle, R.M.,
327 Kahre, M.A., Campbell, B.A., Carter, L.M. and Smith, I.B., 2011. Massive CO₂ ice deposits
328 sequestered in the south polar layered deposits of Mars. *Science*, 332(6031), 838-841.
329
330 Pierrehumbert, R.T. (2010). *Principles of planetary climate*. Cambridge University Press.
331
332 Ramirez, R. M., and J. F. Kasting. Could cirrus clouds have warmed early Mars?, *Icarus* 281
333 (2017): 248-261.
334
335 Ramirez, R.M., 2017. A warmer and wetter solution for early Mars and the challenges with
336 transient warming. *Icarus*, 297, 71-82.
337
338 Richardson, M. I., A. D. Toigo, and C. E. Newman. PlanetWRF: A general purpose, local to
339 global numerical model for planetary atmospheric and climate dynamics. *J. Geophys. Res. -*
340 *Planets* 112 (2007), E09001.
341

342 Salmi, B. 3D-printing a rocket. *IEEE Spectrum* 56, no. 11 (2019): 22-29.
343
344 Seinfeld, J., & S. Pandis (2016), *Atmospheric chemistry and physics*, 3rd edn., Wiley.
345
346 Spiga, A., F. Forget, S. R. Lewis, and D. P. Hinson. Structure and dynamics of the convective
347 boundary layer on Mars as inferred from large-eddy simulations and remote-sensing
348 measurements. *J. Geophys. Res.* 136, no. 647 (2010): 414-428.
349
350 Streeter, P.M., S.R. Lewis, M.R. Patel, J.A. Holmes, and D.M. Kass. Surface warming during the
351 2018/Mars year 34 global dust storm. *Geophys. Res. Lett.* 47, no. 9 (2020): e2019GL083936.
352
353 Toigo, A. D., C. Lee, C. E. Newman, and M. I. Richardson. The impact of resolution on
354 the dynamics of the martian global atmosphere: Varying resolution studies with the
355 MarsWRF GCM. *Icarus* 221, no. 1 (2012): 276-288.
356
357 Turbet, M., C. Gillmann, F. Forget, B. Baudin, A. Palumbo, J. Head, and Ö. Karatekin, 2020,
358 The environmental effects of very large bolide impacts on early Mars explored with a
359 hierarchy of numerical models, *Icarus* 335, 113419.
360
361 Van Vleck, J. H., F. Theory of radar reflection from wires or thin metallic strips. *Journal of*
362 *Applied Physics* 18, no. 3 (1947): 274-294.
363
364 Wolff, M. J., and R. T. Clancy. Constraints on the size of Martian aerosols from
365 Thermal Emission Spectrometer observations. *J. Geophys. Res. - Planets* 108, no. E9 (2003).
366
367 Wordsworth, R., L. Kerber, and C. Cockell. Enabling Martian habitability with silica aerogel
368 via the solid-state greenhouse effect. *Nature Astronomy* 3, no. 10 (2019): 898-903.

369 **Supplementary Material.**

370

371 **Methods.**

372

373 **1. Calculation of optical properties of nanorods.**

374

375 Simple calculations (e.g. Van Vleck et al. 1947) suggest that 9 μm long conductive nanorods
376 with a 60:1 aspect ratio would have a strong and broad extinction in the $\sim 22 \mu\text{m}$ spectral
377 window. To test this, we carried out finite-difference time domain simulations (FDTD: 3D
378 Electromagnetic Simulator). First, we verified that the FDTD simulations reproduce
379 Mie theory for water ice spheres (Iwabuchi & Yang 2011) (Fig. S1). The nanorod FDTD
380 simulations use a pulse of light whose interaction with the simulated nanoparticle
381 is Fourier-decomposed to obtain the λ -dependence of the absorption and scattering cross
382 sections as well as the scattering asymmetry. The representation of the angular distribution
383 of scattered light by a single parameter, the scattering asymmetry, is standard in climate
384 modeling (e.g., Pierrehumbert 2010). 75 wavelengths, approximately log-uniformly spaced
385 from 0.24-55 μm , are obtained (Table S1). We used refractive indices for Fe from Querry
386 (1985), and for Al from Rakić (1995). Cahill et al. (2019) suggest that Fe refractive indices
387 obtained prior to their own work might be affected by Fe-oxidation, but as Mars' atmosphere
388 is $\sim 0.1\%$ O_2 some degree of oxidation is inevitable, so this is acceptable. Implementation
389 involved combining three different simulations for different λ ranges, for computational
390 feasibility. 75 simulations were carried out for the 9 μm long nanorod, corresponding
391 to the product of 5 orientations in θ , 5 orientations in φ (0° , 30° , 45° , 60° , and 90° , for both
392 angles), and three λ ranges. Here, θ corresponds to rotations in the E-H plane and the other
393 rotation is termed φ (k-E plane, symmetric and similar to k-H plane) (Fig. S2).
394 Far-field methods were employed to obtain the scattering phase function. We anticipate that
395 actual nanorods will have circular cross-sections. Because of computational limitations
396 associated with the FDTD approach, we model a nanorod with square cross-section, but find
397 that switching between circular and square cross-sections makes negligible difference
398 to the calculated optical properties (Fig. S3).

399

400 As expected, the simulated nanorods showed strong, broad absorptions near 22 μm (Fig. 1),
401 supporting their suitability for Mars warming. This is consistent with previous work on
402 Ag nanorods (Neubrech & Pucci 2012). The wavelength of the absorption peak is slightly
403 longer than double the rod length, due to plasma effects (Novotny 2007). In order to average
404 over orientations (Fig. S4), rod orientation was uniformly sampled on the sphere relative to
405 the incident electric field vector (~ 1000 samples between 0° and 90° for both angles)
406 and optical properties interpolated using a spline in the grid of 25 computed orientations
407 for each λ . The orientations of nanorods in the atmosphere are assumed to be random
408 and uniform, hence averaging over a spherically equidistant grid of orientations would result
409 in proper orientation-averaged characteristics. We found (minor) infrared back-scattering
410 in these simulations, but zeroed it out in the climate simulations. A sensitivity test using

411 the 3D model showed that this choice makes little difference (~ 0.3 K) to the calculated
412 temperatures.

413
414 To check the interpolation accuracy, we did check runs on multiple intermediate points.
415 (Fig. S5). When the rod is viewed nearly end-on, the interpolation results grow less accurate.
416 However, end-on geometries are infrequently encountered, and at the higher angles,
417 the scattering and absorption cross-sections are significantly smaller, so the effect of these
418 points on the overall orientation average is insignificant. To check the simulation accuracy,
419 we did a check run increasing the resolution across the width of the nanorod from 8
420 simulation mesh points (20 nm spacing) to 10 simulation mesh points (16 nm spacing,
421 finding negligible differences (Fig. S6).

422
423 We also did calculations for 7.5 μm -long Fe nanorods with cross-section $0.08 \mu\text{m} \times 0.08 \mu\text{m}$,
424 finding peak extinction around 20 μm (Fig. S7), and less climate warming per nanorod,
425 but more climate warming per kg of nanorods. An optimal warming approach might use a
426 mix of rods of different lengths. Moreover, we find that the total extinction (absorption plus
427 scattering) for Al nanorods is the same as for Fe nanorods (Fig. S8), even though the density
428 of Al is three times less than that of Fe. This suggests that further research might yield further
429 improvements in the effectiveness of warming.

430
431 **2. Calculation of the surface-warming effect of the nanorods using 1D climate model.**
432 Our single-column radiative-convective climate model (RCM) subdivides atmospheres into
433 multiple vertical log-layers (we implement 201 layers here) that extend from the ground
434 to the top of the atmosphere (1×10^{-5} bar here) (e.g. Ramirez 2017). The RCM has 55 infrared
435 and 38 solar spectral intervals (Kasting et al. 1993). The model applies a standard moist
436 convective adjustment (e.g. Manabe and Wetherald 1967). Should tropospheric radiative
437 lapse rates exceed their moist adiabatic values, the model relaxes to a moist H_2O adiabat
438 at high temperatures or to a moist CO_2 adiabat when temperatures are low enough for CO_2
439 to condense. The RCM implements a standard solar spectrum (Thekaekara 1973). For
440 present Mars (solar flux = 585 W/m^2), we assume a typical stratospheric temperature of
441 155 K and a surface albedo of 0.22 (e.g. Ramirez and Kasting 2017). The atmospheric
442 pressure is a Mars-like 650 Pa with an assumed acceleration due to gravity of 3.73 m/s^2 .
443 Although we prescribe a tropospheric relative humidity of 50%, our results are insensitive
444 to this parameter. The baseline mean surface temperature of the resultant pure CO_2
445 atmosphere (without nanorods) is 218 K. Given the lack of topography, surface ice, etc., in
446 the 1D model, this value is somewhat higher than the ~ 205 K computed by MarsWRF (see
447 Table S2). For comparison, Mars' observed global mean surface temperature is 202 K
448 (Haberle 2013).

449
450 Following Ramirez (2017) and Ramirez and Kasting (2017), we calculate the wavenumber-
451 dependent optical depths (τ) for the nanorods from the following expression:

452
453
$$\tau = 3 Q_{\text{eff}} NRC \Delta z / (4 r \rho) \quad (2)$$

454
455 Here, NRC is the nanorod content (g/m^3) and Δz is the path length. This equation differs from
456 (1) only in that the optical depth is integrated over all nanorod heights and across
457 all wavenumbers, not just in the spectral window. The nanorods are well-mixed throughout
458 the atmosphere (up to 35 km) above the imposed 500 Pa nanorod-layer base and so NRC
459 was assumed to scale linearly with the local pressure. We computed the radius of the sphere
460 with the equivalent nanorod volume, which yields an effective nanorod particle radius
461 of $\sim 0.38 \mu\text{m}$ for the $9 \mu\text{m}$ nanorods.

462
463 Within the 1D model framework, we implement a simple procedure to calculate nanorod
464 warming. For each assumed nanorod optical depth, we find the surface temperature
465 that yields stratospheric energy balance (i.e. the net outgoing and net incoming fluxes must
466 balance each other) (Figs. S16-S17).

467 468 **3. Calculation of the surface-warming effect of the nanorods using 3D climate model.** 469

470 The FDTD output is interpolated to 2000 log-uniformly spaced λ 's. We set optical properties
471 at $\lambda > 55 \mu\text{m}$ equal to those at $55 \mu\text{m}$ (Fig. S9). This approximation is acceptable, because
472 extinction ($\text{W}/\text{m}^2/\mu\text{m}$) is minor at such long λ . MarsWRF uses a two-stream radiation code
473 (e.g. Mischna et al. 2012, Kite et al. 2021). Radiative transfer calculations include both gas
474 (for this work, CO_2) and aerosol (for this work, natural dust, nanorods, and CO_2 ice) radiative
475 effects. This implementation of MarsWRF uses Planck-weighted averaging to bin down
476 high-spectral-resolution optical properties. The blackbody temperature used for
477 the Planck-weighted averaging is 6000K for solar bands (6 bins from $0.24\text{-}4.5 \mu\text{m}$, with bin
478 edges at $0.24, 0.40, 0.8, 1.31, 1.86, 2.48, 3.24,$ and $4.5 \mu\text{m}$), and 215K for the thermal infrared
479 bands (6 bins from $4.5\text{-}1000 \mu\text{m}$, with bin edges at $4.5, 8.0, 12.0, 14.1, 16.0, 24.0, 60,$
480 and $1000 \mu\text{m}$) (Fig. S9). Thermal equilibrium between gas and dust is assumed. We neglect
481 radiation pressure, magnetic effects, quantum size effects, and temperature dependence
482 of the optical constants.

483
484 In the fixed-cloud runs, present-day Mars values are used for orbital parameters, surface
485 albedo, and surface thermal inertia. Mars' southern summer solstice occurs near perihelion,
486 so (by Kepler's second law) northern summer is long and relatively cool, and southern
487 summer is short and warm relative to annual average (Figs. S10-S12). Water vapor
488 abundance in the atmosphere is fixed to zero, which is conservative in that water vapor
489 radiative feedback would increase warming. A prescribed natural dust aerosol distribution
490 is imposed corresponding to the Mars Climate Database MGS-dust-scenario
491 (Montabone et al. 2012), giving an average dust optical depth of 0.20 (peaking at 0.43 during
492 southern summer). Natural dust aerosol warms the atmosphere but lowers daytime surface
493 temperature. The artificial-aerosol layer is parameterized by a layer-base pressure (in Pa),
494 a layer vertical thickness (in units of model levels), and the nanorod orientation-averaged
495 optical depth at a reference λ ($0.67 \mu\text{m}$). Because the model levels are specified
496 in σ coordinates (where $\sigma = P/P_{\text{surf}}$), the aerosol layer is physically more compact over the

497 poles because low temperatures compact the air column. We refer to the altitude away from
498 the poles below which 95% of the particles are contained as the "aerosol layer top height".
499 The nanorod mixing ratio is assumed to be uniform within the nanorod layer (Fig. S13).
500 We prescribe a layer-base level of 500 Pa and vary the layer thickness. Buffering by latent
501 heat implies that melting either ice cap to form seas would take at least centuries.
502

503 Settling for a 0.1 μm -radius particle for 1 scale height at Mars surface pressure takes 3 years
504 (Murphy 1990). Extrapolation to nanorods with radius 0.04 μm suggests settling times
505 that are similar or greater (depending on material type). Increase of Mars' atmospheric $p\text{CO}_2$
506 under warming will decrease the Knudsen number and hinder dust settling. One-pass
507 settling rates are much slower than that of natural Mars dust, and effective particle lifetime
508 will be longer due to re-entrainment.
509

510 The runs presented here use a horizontal resolution of $5.625^\circ \times 3.75^\circ$, corresponding to
511 a grid of 64 points in longitude \times 48 points in latitude. A 40-layer vertical grid is used, using
512 a modified- σ (terrain-following) coordinate. The dynamical timestep varies between runs
513 but is never longer than 1-min. The planetary boundary layer scheme is based on that in
514 Fonseca et al. (2018), and the surface layer uses a Monin-Obukhov scheme. Runs are
515 initialized from a cold state and continue until the simulated annual seasonal cycle is highly
516 repeatable from year to year. We found that runs require only a single year of spin-up
517 adjustment, as modern Mars, lacking seas, has low effective thermal inertia. Mean wind
518 speed ~ 30 m above the surface increases from 8 m/s in the no-nanorods case to 14 m/s in
519 the Fig. 2a (with-nanorods) case, which would stir up more dust (and nanorods). Daytime
520 near-surface turbulence on Mars is sufficient to loft dust (and therefore nanorods) released
521 at 10-100m altitude at all latitudes for $P > 6$ mbar. Sensitivity tests adjusting model resolution,
522 and varying nanorod distribution and other parameters are listed in Table S3.
523

524 For the no-nanorods case (Fig. 2b), the global and annual average shortwave radiation
525 reaching the surface is 133.1 W/m^2 (119.7 W/m^2 direct beam and the remainder
526 diffuse/scattered), of which 104.2 W/m^2 is absorbed with the rest being reflected.
527 The spatially- and time-averaged surface albedo, including ice, is 0.237. The global/annual
528 average longwave radiation at the surface (greenhouse effect) is 23.9 W/m^2 . The
529 global/annual average longwave emission from the surface is 125.4 W/m^2 . The mismatch of
530 -2.7 W/m^2 is caused by limited output sampling, fluxes into the surface (e.g. CO_2
531 condensation, conduction), and model imprecision. For the with-nanorods case shown in
532 Fig. 2a, the global and annual average shortwave radiation reaching the surface is 71.2 W/m^2
533 (44.0 W/m^2 direct beam), of which 56.3 W/m^2 is absorbed with the rest being reflected.
534 The spatially- and time-averaged surface albedo, including ice, is 0.207. A greater fraction of
535 sunlight is absorbed due to reduction in reflective seasonal CO_2 ice. The global/annual
536 average longwave radiation at the surface (greenhouse effect) is 190.2 W/m^2 .
537 The global/annual average longwave emission from the surface is 244.7 W/m^2 . The
538 mismatch of -1.9 W/m^2 (i.e., surface temperature under-stated relative to radiative fluxes) is

539 caused by limited output sampling, fluxes into the surface (e.g. CO₂ condensation,
540 conduction), and model imprecision.

541
542 The runs shown in Fig. 2c correspond to optical depths at $\lambda = 0.67 \mu\text{m}$ of {0, 0.125, 0.25, 0.5,
543 0.75, 1, 1.5, 2}. Details for selected values of are given in Fig. S14. The conversion factor is
544 545 mg/m² for one optical depth. Optical depths in the spectral windows are much greater
545 than at 0.67 μm (Fig. 1). Output was sampled at 260 equally spaced intervals per Mars year.
546 This provides (deliberately aliased) sampling of the day-night cycle during each season at
547 each longitude and latitude. A sensitivity test using 1300 output steps showed negligible
548 (≤ 0.1 K) differences in both annual-average and seasonal warming (Table S3). Mars'
549 atmosphere is thin, with low thermal inertia and limited ability to transport heat laterally,
550 and the tests with artificial imposed patchy or unsteady nanorod distribution show that
551 the corresponding warming is sharply confined in space and time. This suggests that it might
552 be possible to enhance warming at preferred latitudes and seasons, by making use of Mars'
553 atmospheric circulation.

554

555 **4. Possible hazards.**

556

557 Natural Mars air is unsafe for humans to breathe because it has almost no oxygen
558 (insufficient for deflagration) and also has a high natural concentration of PM 2.5 (Mars
559 mineral aerosol dust). The nanorod density is $\sim 10 \mu\text{g}/\text{m}^3$, which would not significantly alter
560 this situation. A more immediate concern is asbestosis, as humans would bring both natural
561 dust and nanoparticles into settlements via airlocks. One way to mitigate this hazard would
562 be to make nanorods that dissolve or fragment in liquid water.

563

564 **5. Comparison to previous work.**

565

566 To our knowledge, the most effective (on a per-unit-mass-in-the-atmosphere basis) Mars
567 warming agent that has been previously been proposed is the "optimal [gas] mix" of
568 Marinova et al. (2005), which is mostly C₃F₈ (molecular mass 188 Da). This gives 37.5 K
569 warming for 1 Pa, which corresponds to $170 \text{ kg}/\text{m}^2 \times (1 \text{ Pa} / 650 \text{ Pa}) \times (\sim 188 \text{ Da} / 44 \text{ Da}) \approx$
570 $1.1 \text{ kg}/\text{m}^2$. This warming is about the same as the nanorod case shown in Fig. 2a, which
571 corresponds to $\sim 400 \text{ mg}/\text{m}^2$ of nanorods. Therefore this nanorod loading (using non-
572 optimized nanoparticles) is $>2000\times$ more effective than the optimal gas mix.

573

574 **Supplementary-Only References**

575

576 Cahill, J., D. T. Blewett, N. V. Nguyen, A. Boosalis, S. J. Lawrence, and B. W. Denevi. Optical
577 constants of iron and nickel metal and an assessment of their relative influences on silicate
578 mixture spectra from the FUV to the NIR. *Icarus* 317 (2019): 229-241.

579

580 Fonseca, R. M., M.-P. Zorzano-Mier, and J. Martín-Torres. Planetary boundary layer and
581 circulation dynamics at Gale Crater, Mars. *Icarus* 302 (2018): 537-559.

582
583 Iwabuchi, H., and P. Yang. Temperature dependence of ice optical constants: Implications for
584 simulating the single-scattering properties of cold ice clouds. *Journal of Quantitative*
585 *Spectroscopy and Radiative Transfer* 112, no. 15 (2011): 2520-2525.
586
587 Kasting, J., Whitmire, D., and Reynolds, R., Habitable Zones Around Main Sequence Stars,
588 *Icarus*, 101 (1993), 108-128.
589
590 Manabe, S. and Wetherald, R.T. (1967), Thermal equilibrium of the atmosphere with a given
591 distribution of relative humidity. *J. Atmospheric Sciences* 24(3), 241-258.
592
593 Millour, E., F. Forget, F. González-Galindo, A. Spiga, S. Lebonnois, S. R. Lewis, L. Montabone et
594 al. The Mars climate database (version 4.3). No. 2009-01-2395. SAE Technical Paper, 2009.
595
596 Neubrech, F., and Annemarie P. Plasmonic enhancement of vibrational excitations in the
597 infrared. *IEEE Journal of selected topics in quantum electronics* 19, no. 3 (2012): 4600809.
598
599 Novotny, L. Effective wavelength scaling for optical antennas. *Phys. Rev. Lett.* 98, no. 26
600 (2007): 266802.
601
602 Rakić, A. D. Algorithm for the determination of intrinsic optical constants of metal films:
603 application to aluminum. *Applied optics* 34, no. 22 (1995): 4755-4767.
604
605 Querry, M. R. Optical constants. US Army Armament, Munitions & Chemical Command,
606 Chemical Research & Development Center (1985).
607
608 Thekaekara, M.P. (1973), Solar energy outside the earth's atmosphere. *Solar energy*, 14(2),
609 109-127.

610 **Supplementary Figures.**

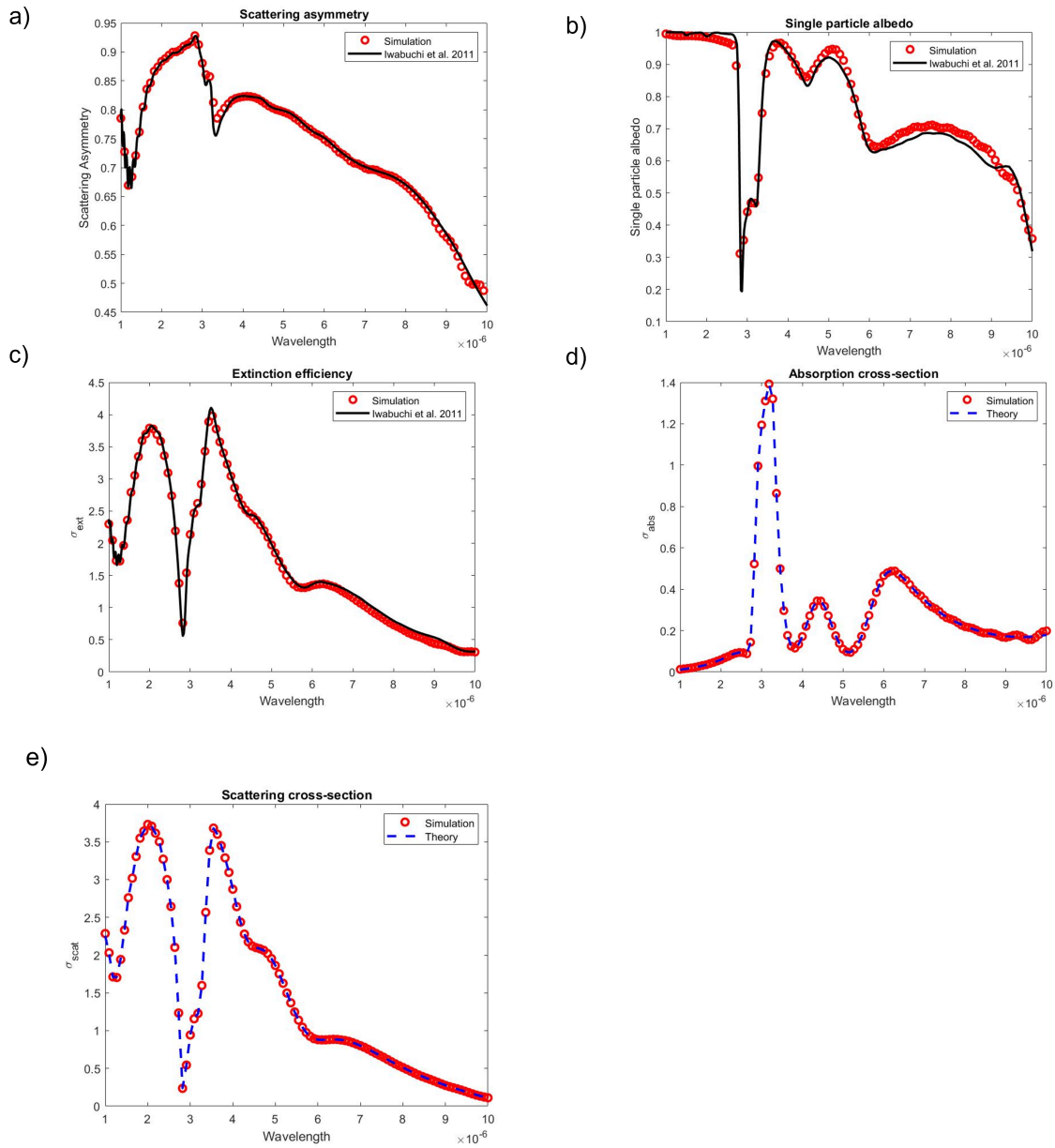


Fig. S1. (a,b,c) Verification of calculations by comparison to Mie-theory results for a water-ice sphere (Iwabuchi & Yang 2011), showing single particle albedo, scattering asymmetry, and extinction efficiency. (d,e) Shows the comparison of analytical Mie scattering results for an ice sphere with simulation outputs.

611

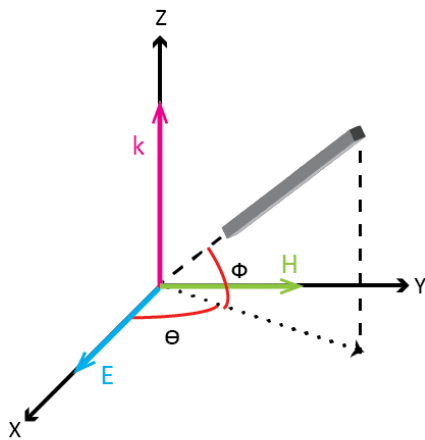


Fig. S2. Illustration showing the definition of the angles θ and ϕ in the FDTD calculation. "k" corresponds to the direction of the propagation of the incident electromagnetic wave. The gray bar corresponds to the nanorod.

612

613

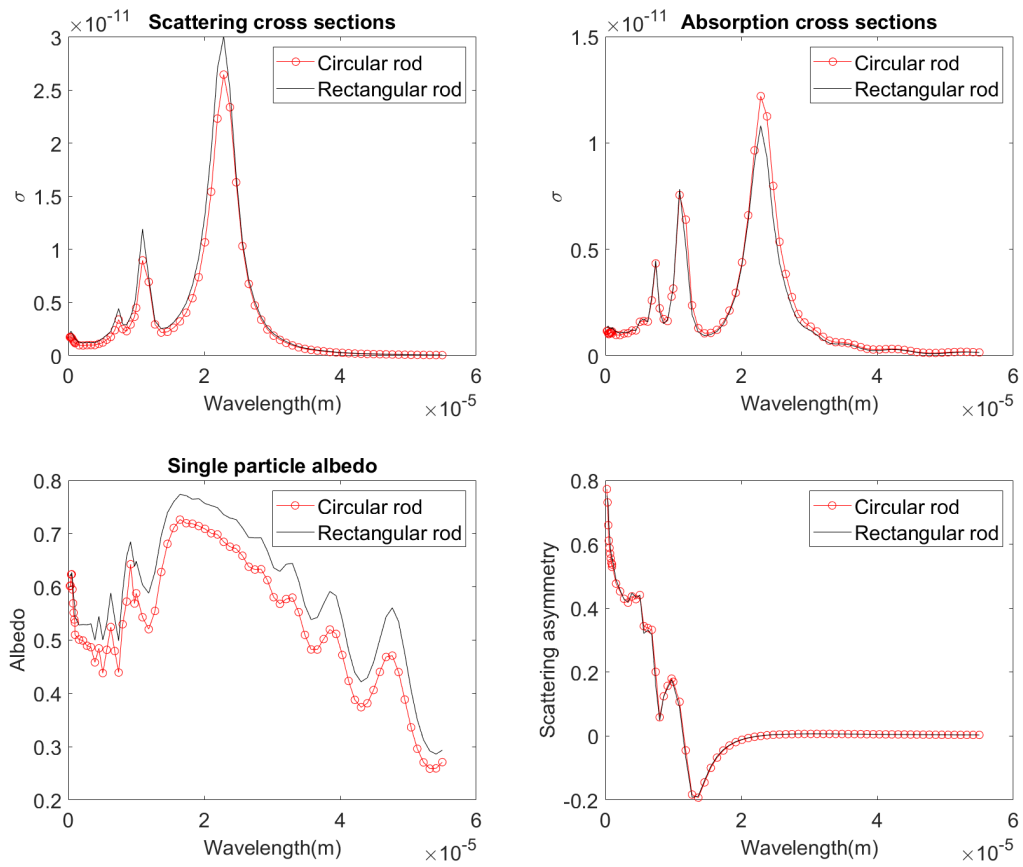


Fig. S3. Switching between a square and circular cross-section for the nanorod has only minor effects on the calculated optical properties. Orientation: $\theta = 45^\circ$, $\varphi = 45^\circ$.

614

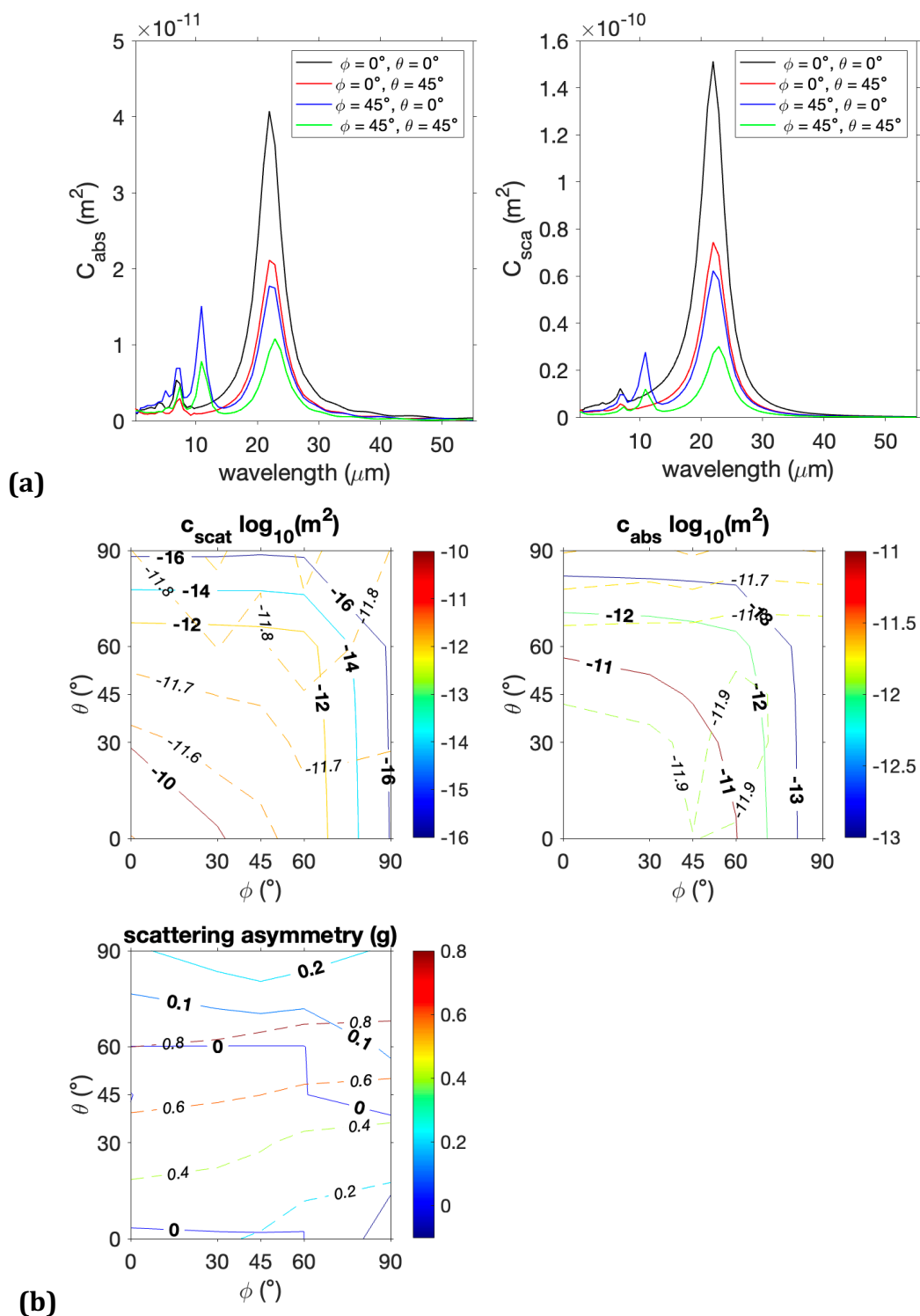
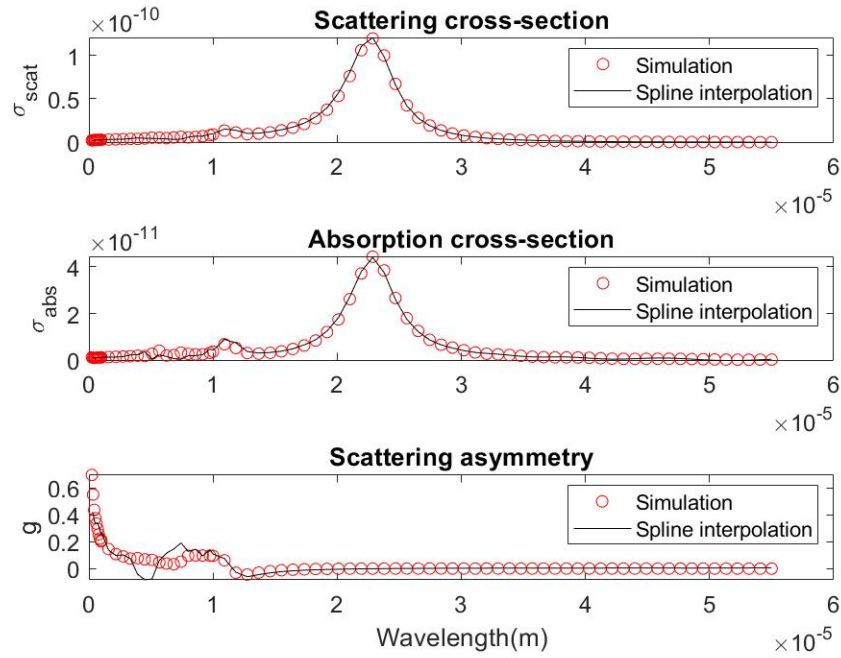
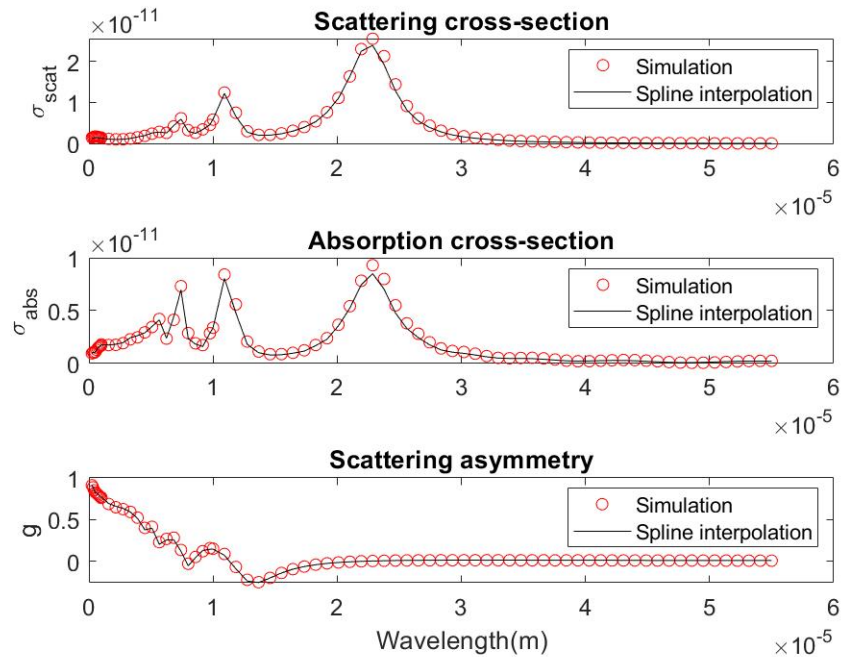


Fig. S4. FDTD output figure, showing orientation dependence of the optical properties of the nanorods. (a) Cross-sections as a function of wavelength. (b) Cross-sections and scattering asymmetry as a function of orientation for wavelengths 21.9 μm (solid lines, bold labels) and 0.70 μm (dashed lines, italic labels).

Results of interpolation and simulation at $\phi=15, \theta=15$ Results of interpolation and simulation at $\phi=60, \theta=15$ 

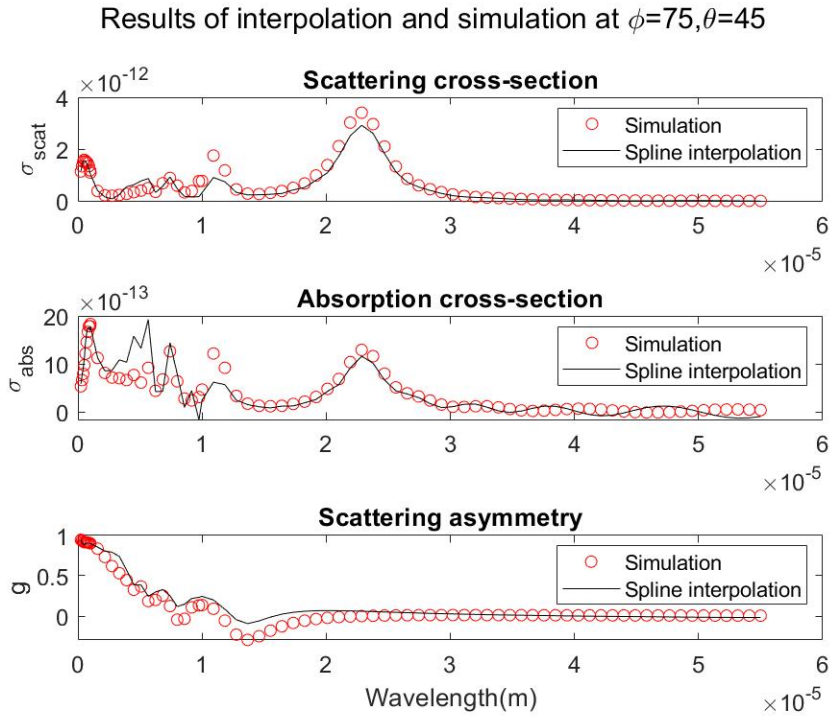
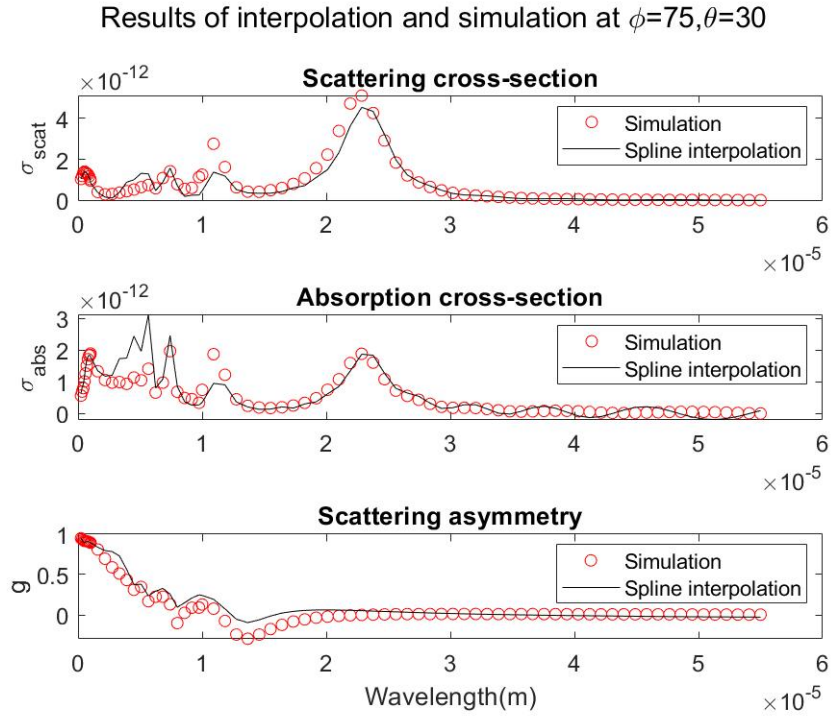


Fig. S5. Results of interpolation check. Units of angles are degrees.

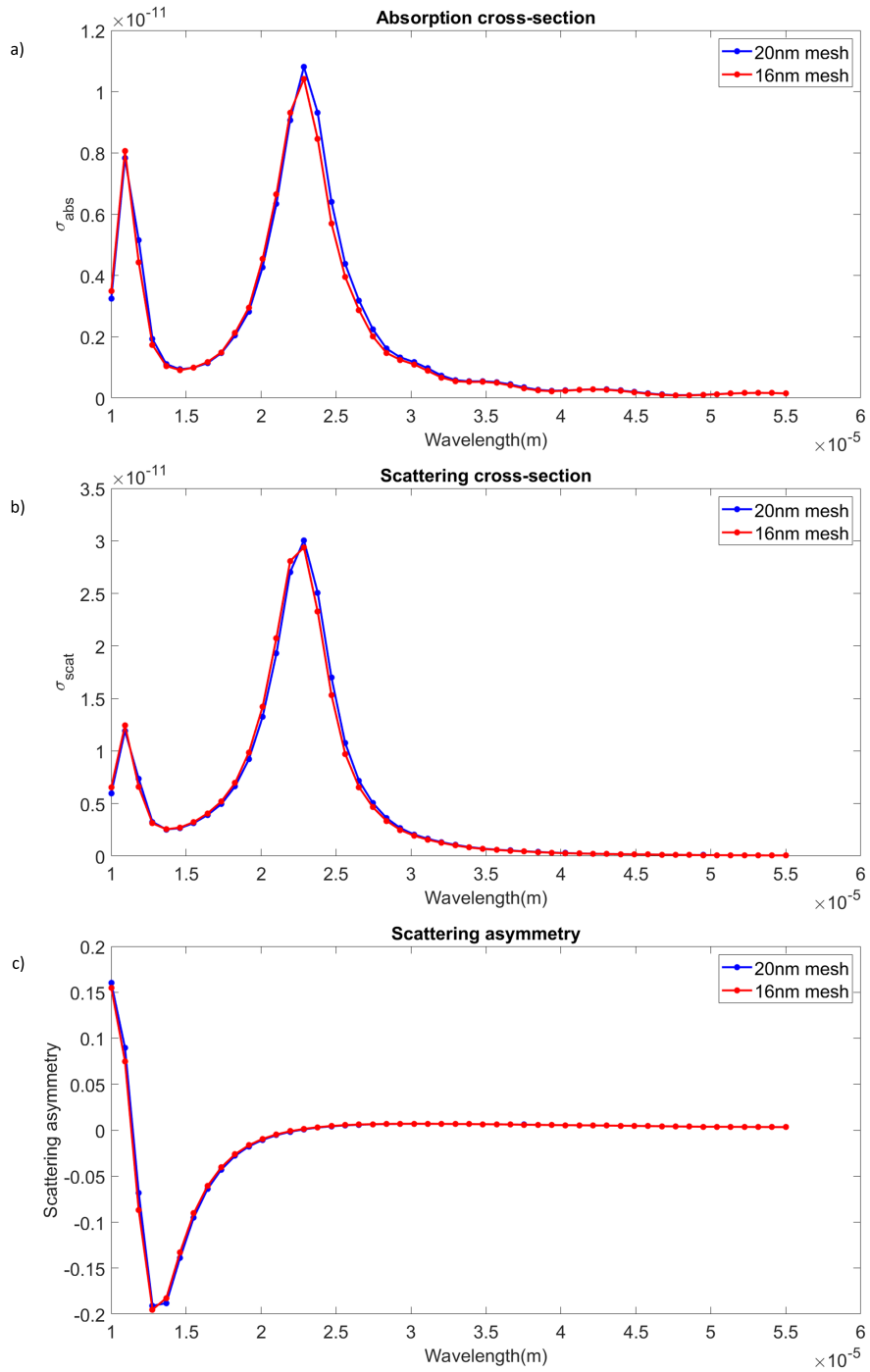


Fig. S6. Sensitivity test showing change in optical properties when mesh resolution is increased (decreasing mesh spacing). Orientation: $\theta = 45^\circ$, $\varphi = 45^\circ$.

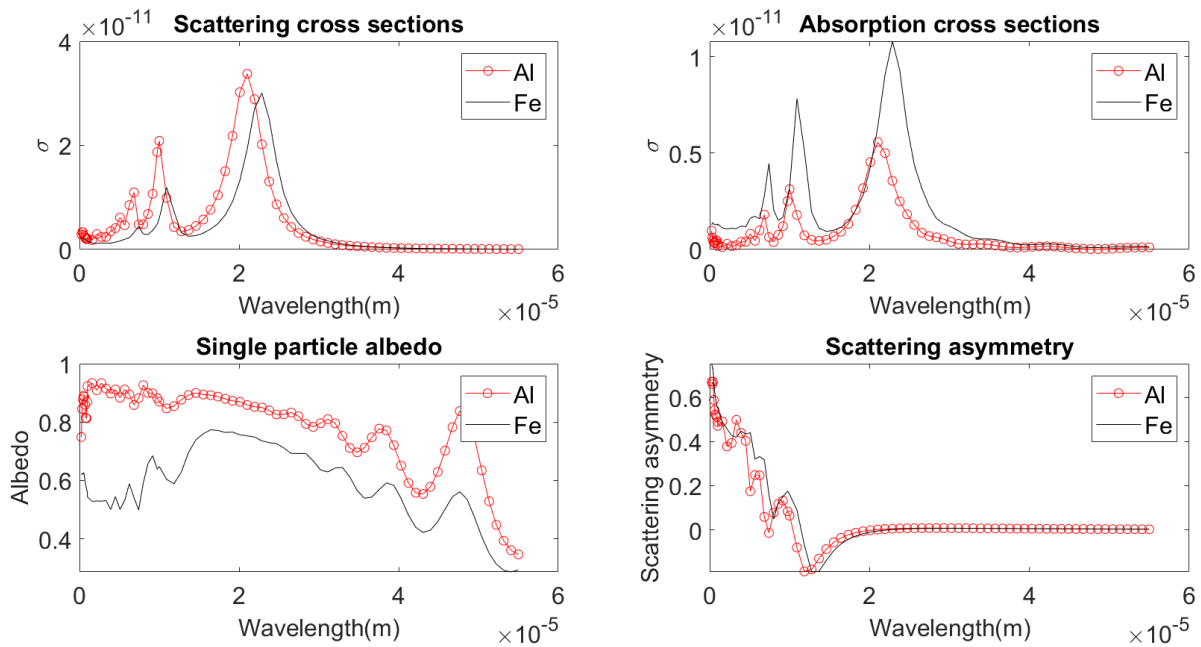


Fig. S7. Showing sensitivity of calculated optical properties to changing nanorod composition (Al vs. Fe). The total extinction cross section (scattering plus absorption) and the location of the resonances remains about the same; a small increase in Al nanorod length would be sufficient to closely match the Fe cross-sections. As Al is $3\times$ less dense than Fe, this suggests Al is more effective on a warming-per-unit-mass basis. Conductive-nanorod size and shape, and not composition, are the main controls on simulated nanorod optical properties. Aluminum material properties are obtained from Rakić (1995). Orientation: $\theta = 45^\circ$, $\varphi = 45^\circ$.

619

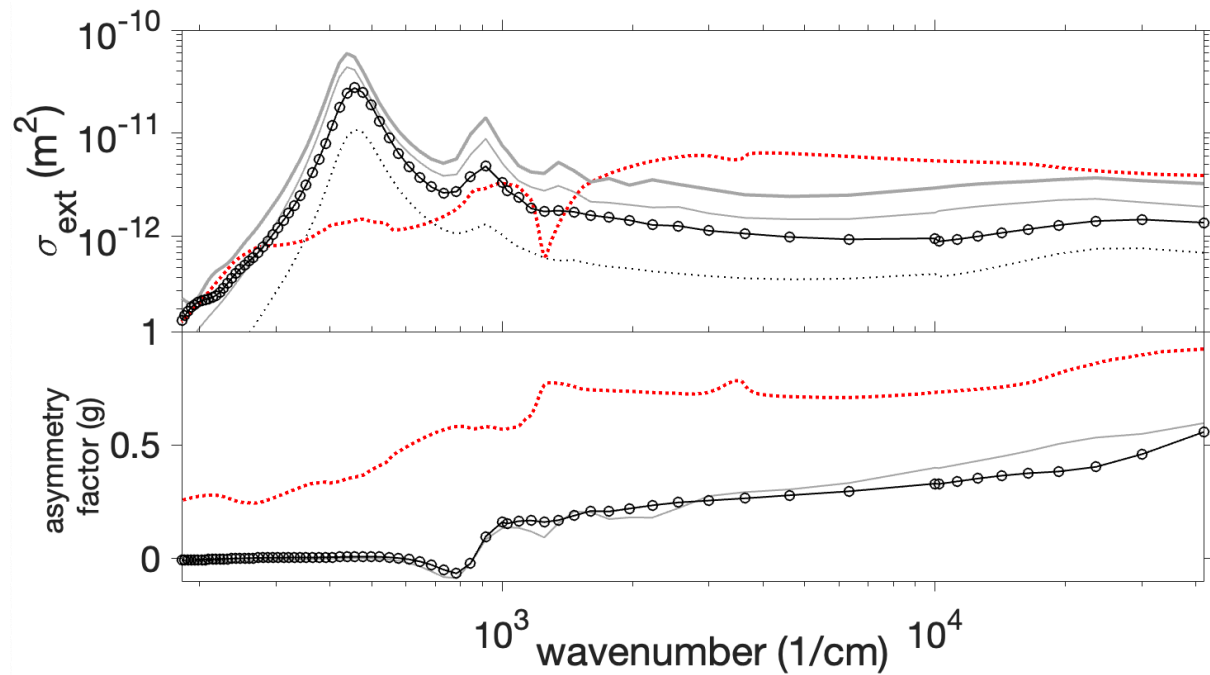


Fig. S8. As Fig. 1, but showing the calculated optical properties for a different particle length and width: specifically, 7.5 μm -long Fe nanorods with cross-section $0.08 \mu\text{m} \times 0.08 \mu\text{m}$. Orientation-averaged optical properties calculated using a 3D Finite-Difference Time-Domain (FDTD) approach. Upper panel: Solid black line corresponds to total extinction, dotted black line to scattering. Lower panel shows scattering asymmetry. Also shown in both panels are spectra for natural dust assuming a log-gaussian particle size distribution centered on 2.5 μm (Wolff & Clancy 2003) (red dotted lines). Thin gray lines correspond to the results for a 9 μm -long Fe nanorod with cross-section $0.16 \mu\text{m} \times 0.16 \mu\text{m}$, as shown in Fig. 1. As expected given its spectrum, the 7.5 μm -long nanorod gives less warming per nanorod in climate simulations (results not shown). However, as it uses $5\times$ less Fe, this design is more effective on a warming-per-unit-mass basis.

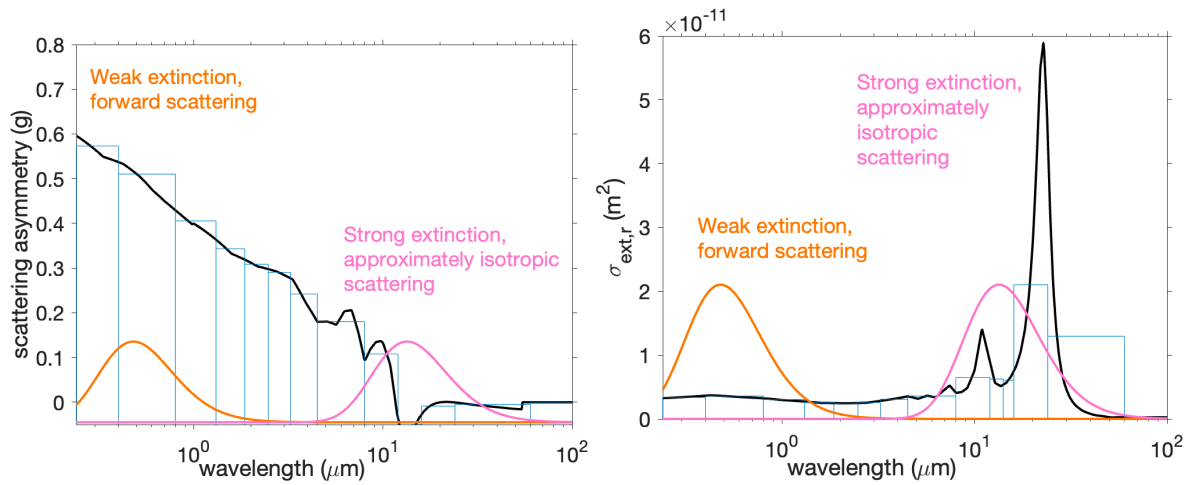


Fig. S9. Showing how the spectra are represented within the 3-D climate model. 4.5 μm marks the separation between solar bins (Planck-weighted using the orange 6000K blackbody curve, normalized $\text{W}/\text{m}^2/\mu\text{m}$ flux density), and thermal IR bins (Planck-weighted using the pink 215K blackbody curve, normalized $\text{W}/\text{m}^2/\mu\text{m}$ flux density). The relative heights of the orange and pink Planck functions are to guide the eye only and have no physical significance.

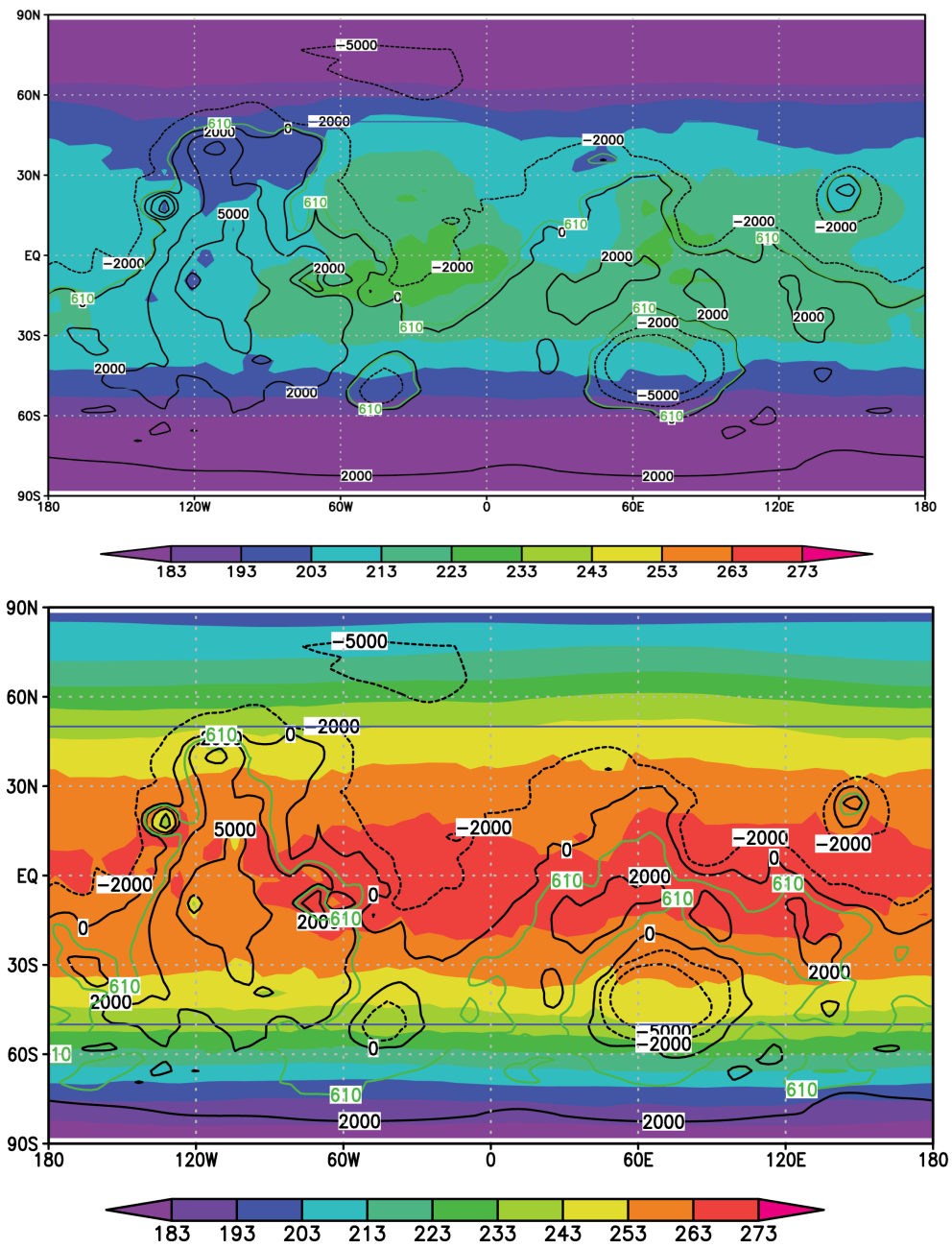


Fig. S10. Annual average temperatures (K) for (top) control simulation without nanorods (i.e., Fig. 2b), and (bottom) warmed case with nanorods (i.e., Fig. 2a). Labeled black contours correspond to topographic elevation in m. Green contour corresponds to 610 Pa mean pressure level. Blue lines: approximate latitudinal (equatorward) extent of ice at <1 m depths.

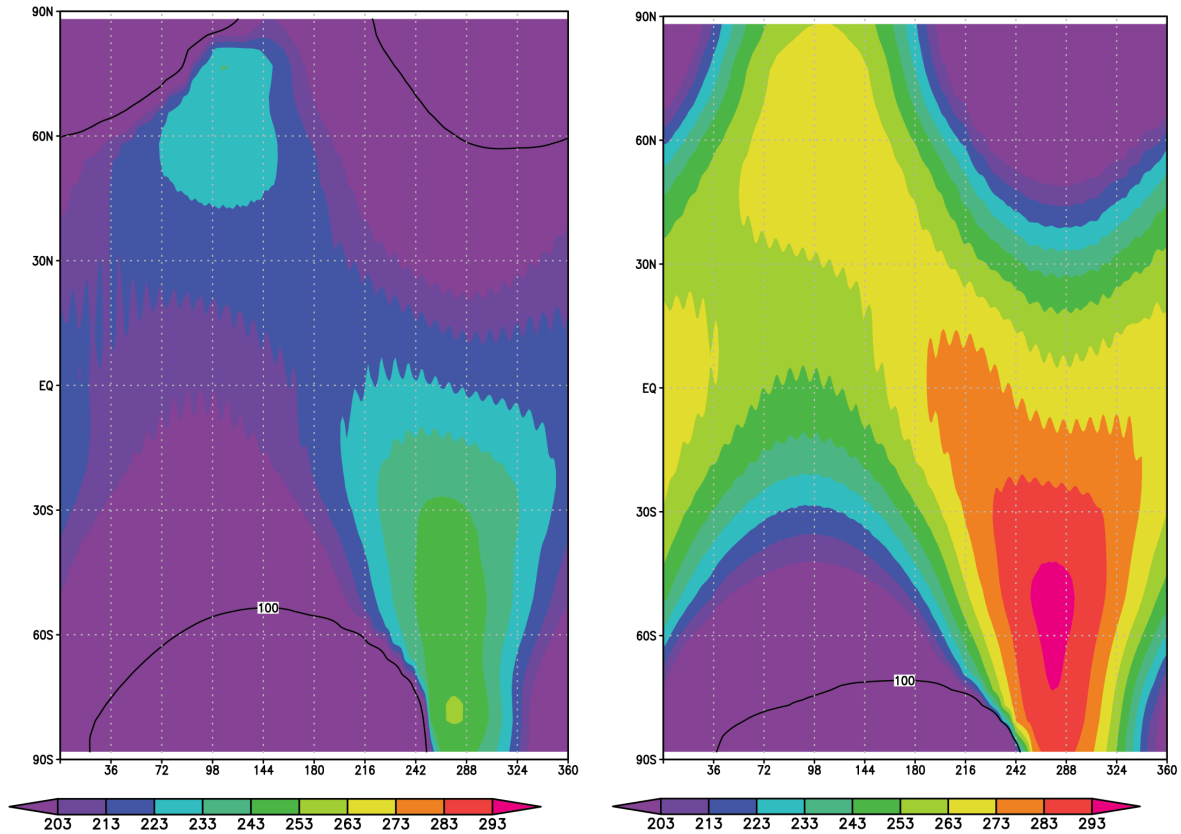


Fig. S11. Seasonal variation of diurnal-average surface temperature (K) for (left) control simulation without nanorods (i.e., Fig. 2b), and (right) warmed case with nanorods (i.e., Fig. 2a), showing longitudinal average surface temperature. Each of the 10 increments on the x-axis, which are equally spaced in time, corresponds to 1/10 of a Mars year (69 Earth days). To make this figure, a 9-point smoother has been used (3 points in time, and 3 points in latitude) in order to damp oscillations associated with aliasing in the sampling of the day-night temperature cycle in the output. The black lines show the limit of significant polar seasonal CO₂ ice.

625

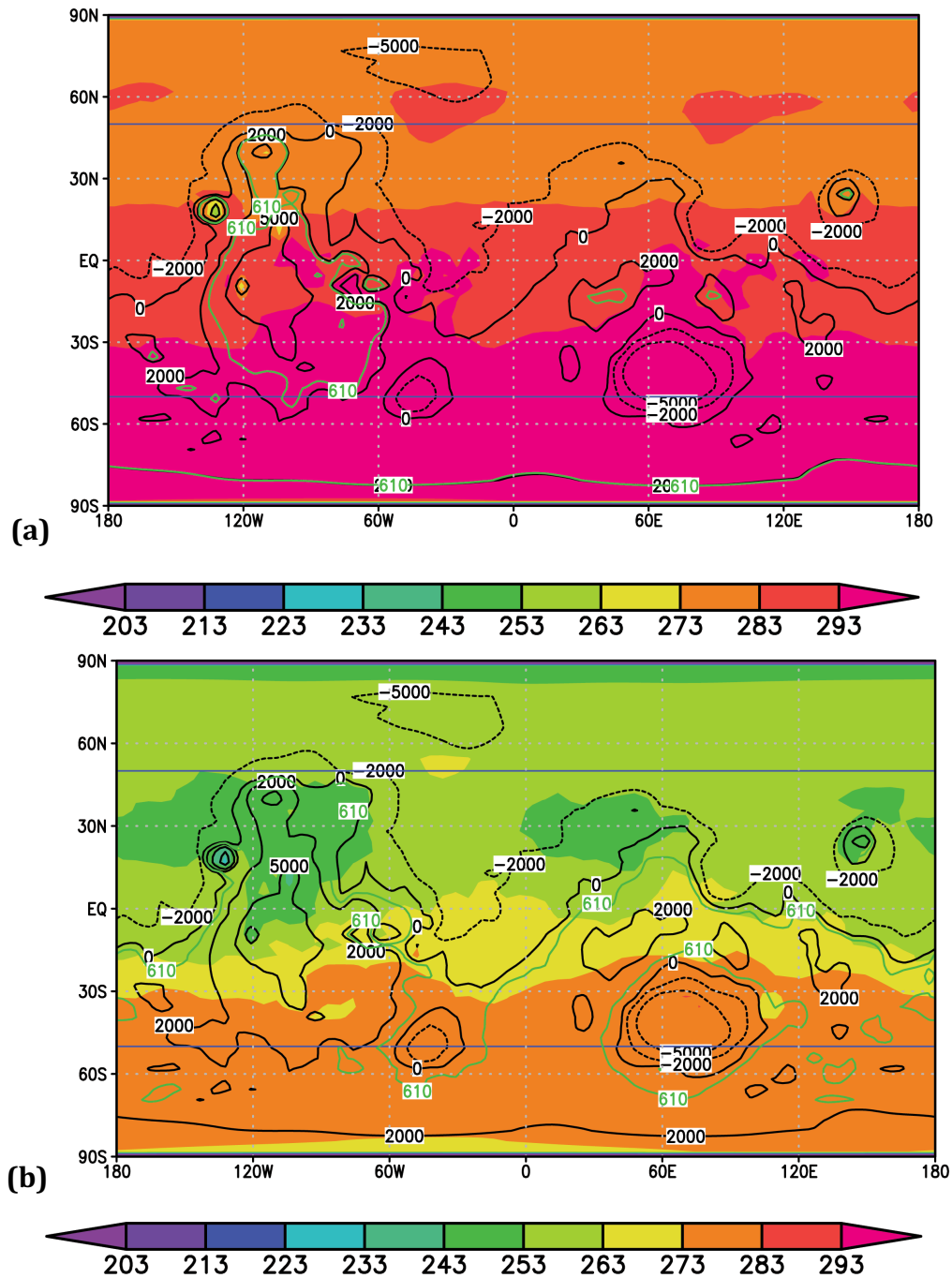


Fig. S12. Sensitivity tests showing how warm-season temperatures vary for different parameter choices. Labeled black contours correspond to topographic elevation in m. Green contour corresponds to 610 Pa mean pressure level. Blue lines: approximate latitudinal (equatorward) extent of ice at <1 m depths. (a) More nanorods ($\tau = 1.5$): the average surface pressure exceeds 610 Pa (green contour) at all locations below +2 km elevation. (b) Fewer nanorods ($\tau = 0.375$).

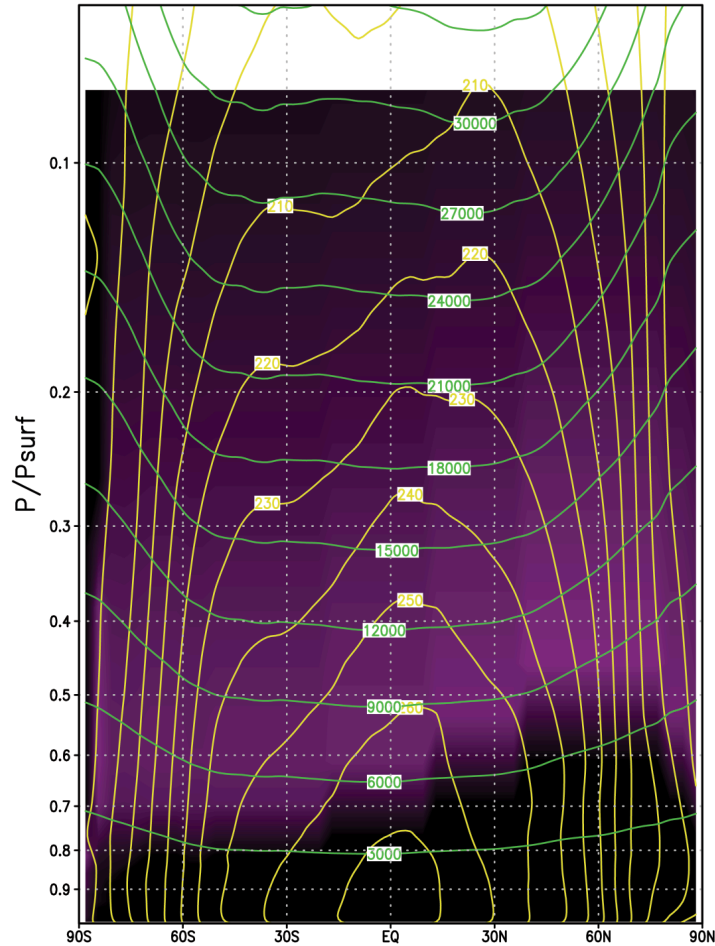


Fig. S13. Cross section of steady (imposed) nanorod layer. The purple shading corresponds to the relative volume density of nanorods. The mixing ratio of nanorods within the purple layer is uniform, but there is more gas closer to the planet's surface so there are also more nanorods lower down. The tenuous part of the nanorod layer extending to high altitude is disproportionately important because of its strong contribution to the greenhouse effect. The Y-axis uses terrain-following σ -coordinates ($\sigma = P/P_{\text{surf}}$), and the cloud lines are tilted down and to the left because the southern hemisphere surface is topographically higher and thus closer to the fixed-pressure base of the nanorod layer. The yellow lines are contours of annual average atmospheric temperature. The green lines are contours of altitude in meters, which bow upwards at the poles where low temperatures compact the gas column.

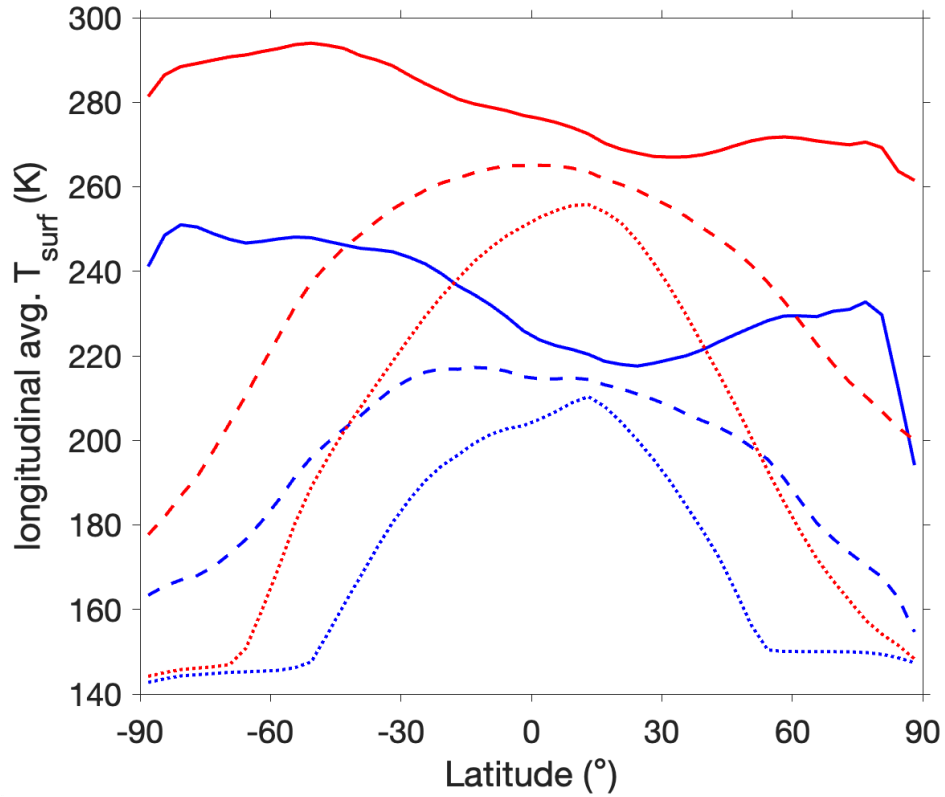


Fig. S14. Summary of the latitudinal and seasonal dependence of surface temperature for (red lines) the 3D model with-nanorods $\tau = 0.75$ case (Fig. 2a), and (blue lines) the 3D model without nanorods (Fig. 2b). Solid line corresponds to the average temperature during the warmest season (~ 70 day period) during the year, dotted line corresponds to the average temperature during the coldest season (~ 70 day period) of the year, and dashed line corresponds to the annual average. The flattening-out of the lines around 145K corresponds to buffering at the frost point of CO_2 .

628

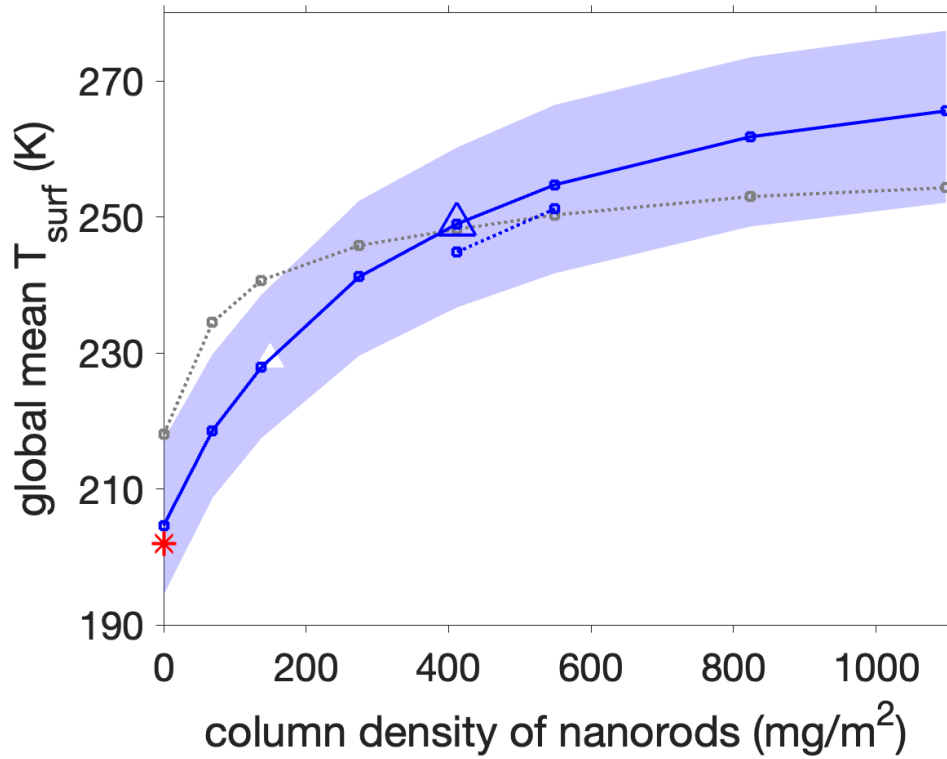
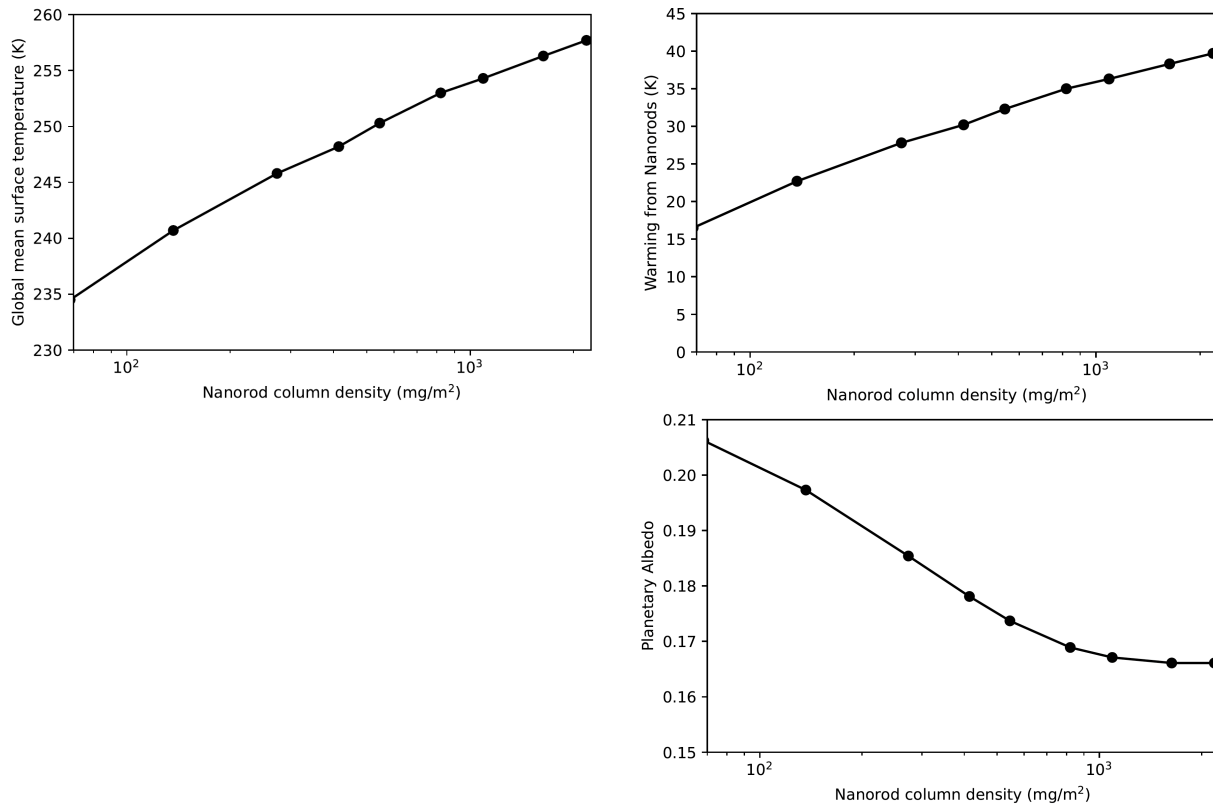


Fig. S15. As Fig 2c, but with a linear x-axis instead of a logarithmic x-axis. Dependence of planet-averaged surface warming on nanorod column mass. Blue triangle corresponds to Fig. 2a, the intersection of the blue line with the zero-nanorods axis corresponds to Fig. 2b, and white triangle marks onset of warm-season temperatures above the freezing point of water at 50°S. Blue corresponds to 3-D results, varying layer-top height between ~35 km (solid line) and ~28 km (dashed line). The blue envelope corresponds to the modeled seasonal range in global mean T_{surf} . Gray corresponds to 1-D results. The red asterisk corresponds to the observed modern Mars value.

631



632 **Fig. S16.** Summary of 1-D climate model output as a function of nanorod column density.
633

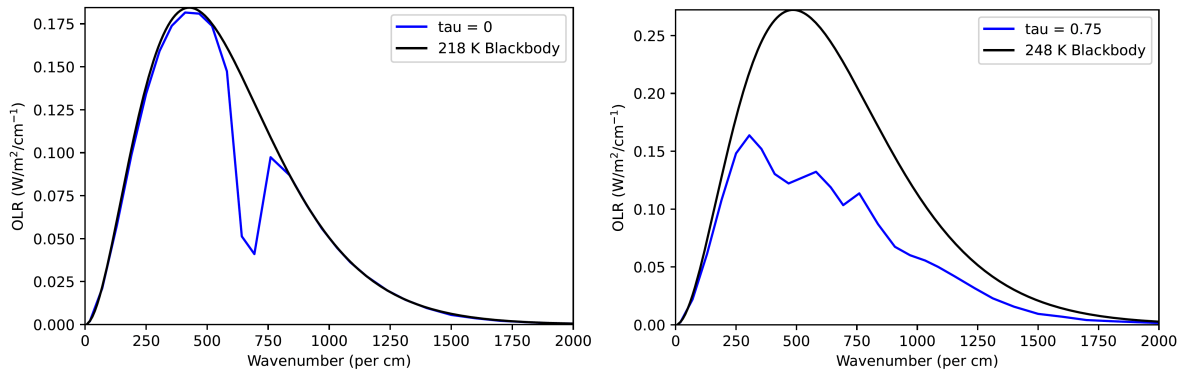


Fig. S17. Outgoing Longwave Radiation (OLR) from the 1D model. Left: the no-nanorods case. Spectral windows are visible as peaks on either side of the CO₂ band which is at 600-800 per cm. Right: the nanorods case with $\tau = 0.75$. Absence of prominent peaks corresponds to closure of the spectral windows.

634

635 **Supplementary Table 1:** orientation-averaged optical properties of nanorods as used in the
 636 climate simulations, corresponding to a 9 μm -long nanorod with cross-section (0.16 \times 0.16) μm .

wavelength ($\times 10^{-4}$ m)	absorption cross- section ($\times 10^{-10}$ m ²)	scattering cross-section ($\times 10^{-10}$ m ²)	asymmetry parameter (g)
0.0024	0.0131	0.0194	0.596
0.0033	0.0133	0.0215	0.549
0.0043	0.0138	0.0232	0.5327
0.0052	0.0131	0.0226	0.505
0.0061	0.0128	0.0214	0.4728
0.007	0.0128	0.0205	0.4492
0.008	0.0127	0.0196	0.4301
0.0089	0.0125	0.0186	0.4131
0.0098	0.0121	0.0177	0.3979
0.01	0.0125	0.017	0.3997
0.0158	0.0104	0.0148	0.3322
0.0217	0.0098	0.0147	0.3041
0.0275	0.0102	0.0152	0.2921
0.0333	0.012	0.0168	0.2745
0.0392	0.0127	0.0193	0.2218
0.045	0.0163	0.0191	0.1798
0.0508	0.0112	0.0203	0.1804
0.0567	0.0152	0.0213	0.1732
0.0625	0.012	0.0217	0.2035
0.0683	0.0163	0.0271	0.206
0.0742	0.0214	0.031	0.1553
0.08	0.013	0.0278	0.0922
0.0858	0.012	0.0302	0.119
0.0917	0.0138	0.0347	0.1344
0.0975	0.0225	0.0452	0.1368
0.1	0.0247	0.0514	0.1327
0.1092	0.0532	0.0886	0.0835
0.1184	0.0359	0.0619	-0.0233
0.1276	0.0165	0.0399	-0.0872
0.1367	0.0125	0.0387	-0.0822
0.1459	0.0126	0.0437	-0.057
0.1551	0.0145	0.0524	-0.0352
0.1643	0.0178	0.0644	-0.0205
0.1735	0.0234	0.0813	-0.0109
0.1827	0.032	0.1081	-0.0053
0.1918	0.0451	0.1489	-0.0018
0.201	0.067	0.2132	-0.0001

0.2102	0.0987	0.3056	0.0006
0.2194	0.1371	0.4119	0.0007
0.2286	0.1553	0.4378	0.0003
0.2378	0.1293	0.3514	-0.0004
0.2469	0.0886	0.2335	-0.0011
0.2561	0.0604	0.1484	-0.0019
0.2653	0.0428	0.099	-0.0028
0.2745	0.0304	0.0691	-0.0037
0.2837	0.0228	0.0495	-0.0044
0.2929	0.0186	0.0369	-0.0051
0.302	0.0154	0.0285	-0.0059
0.3112	0.0124	0.0224	-0.0066
0.3204	0.0103	0.0179	-0.0072
0.3296	0.0089	0.0145	-0.0077
0.3388	0.008	0.0119	-0.0081
0.348	0.007	0.0099	-0.0085
0.3571	0.0061	0.0084	-0.009
0.3663	0.0054	0.0071	-0.0095
0.3755	0.0049	0.0061	-0.01
0.3847	0.0045	0.0052	-0.0104
0.3939	0.0041	0.0046	-0.0108
0.4031	0.0036	0.004	-0.0112
0.4122	0.0032	0.0035	-0.0115
0.4214	0.0029	0.0031	-0.0119
0.4306	0.0027	0.0028	-0.0123
0.4398	0.0027	0.0025	-0.0127
0.449	0.0027	0.0022	-0.0132
0.4582	0.0026	0.002	-0.0136
0.4673	0.0024	0.0018	-0.0139
0.4765	0.0021	0.0017	-0.0143
0.4857	0.0018	0.0015	-0.0146
0.4949	0.0015	0.0014	-0.0149
0.5041	0.0013	0.0012	-0.0151
0.5133	0.0012	0.0011	-0.0153
0.5224	0.0012	0.001	-0.0155
0.5316	0.0013	0.0009	-0.0156
0.5408	0.0015	0.0009	-0.0158
0.55	0.0017	0.0008	-0.016

638 **Supplementary Table 2.** Summary of climate model output.

Optical depth (τ) at $\lambda = 0.67 \mu\text{m}$	Nanorod column mass (mg/m^2)	1-D temperature output, global mean (K)	3D temperature output		
			3-D global mean temperature (K)	50°N warm-season temperature (K)	50°S warm-season temperature (K)
0	0	218.0	204.6	228.8	250.3
0.125	68.4	234.5	218.6	241.2	262.2
0.25	136.6	240.7	227.9	250.9	271.9
0.5	273.8	245.8	241.2	263.2	285.9
0.75	414.3	248.2	249.0	270.9	294.0
1	545.1	250.3	254.7	275.7	299.3
1.5	820.8	253.0	261.8	281.5	304.9
2	1091.1	254.3	265.6	285.0	307.1

639
640 **Supplementary Table 3.** Summary output for additional sensitivity tests using 3D model.

Description	Optical depth (τ) at $\lambda = 0.67 \mu\text{m}$	3D temperature output		
		3-D global mean temperature (K)	50°N warm-season temperature (K)	50°S warm-season temperature (K)
<i>Reference</i>	0.75	249.0	270.9	294.0
Lower cloud top	0.75	244.8	270.6	289.5
Lower cloud top	1	251.2	275.6	297.1
2× atmospheric pressure (≈ 12 mbar)	0.75	252.7	269.9	290.1
Nanorods extend only from 45°S - 45°N	0.75	237.7	230.5	253.2
Nanorods only active from $L_s = 180 - 360$, passive at other seasons	0.75	224.9	229.2	293.3
5× greater output frequency	0.75	249.0	270.8	294.0
2× smaller numerical timestep	0.75	249.5	271.0	293.5
Thinner cloud (200 Pa base, 8 levels)	0.75	248.7	269.3	290.9
96×72 spatial grid in model (vs. default of 64×48)	0.75	250.5	271.1	292.9

641